Global and Planetary Change 232 (2024) 104343

Contents lists available at ScienceDirect

Global and Planetary Change

journal homepage: www.elsevier.com/locate/gloplacha

Evidence for variable provenance of Mercury anomalies during the Smithian–Spathian (Olenekian)

Oluwaseun Edward [a,*], Marc Leu [b], Hugo Bucher [b], Sandrine Le Houedec [c], Franziska Blattmann [a], Christian Vérard [c], Thierry Adatte [d], Aymon Baud [d], Jeroen E. Sonke [e], Torsten Vennemann [a]

[a] Institute of Earth Surface Dynamics, Géopolis, University of Lausanne, CH-1015 Lausanne, Switzerland
[b] Paleontological Institute and Museum, University of Zurich, Karl-Schmid-Strasse 4, 8006 Zürich, Switzerland
[c] Department of Earth Sciences, Université de Genève, Rue des Maraîchers 13, CH-1205 Genève, Switzerland
[d] Institute of Earth Sciences, Géopolis, University of Lausanne, CH-1015 Lausanne, Switzerland
[e] Observatoire Midi-Pyrénées, Géosciences Environnement Toulouse, Université Paul Sabatier Toulouse 3, 14 Avenue Edouard Belin, 31400 Toulouse, France

ARTICLE INFO

Editor: Maoyan Zhu

Keywords:
Early Triassic
Volcanism
Siberian Traps
Mercury anomalies
SSB

ABSTRACT

Mercury (Hg) enrichment recorded in Smithian to Spathian (Olenekian) marine sedimentary successions has been used to link putative renewed Siberian Traps Large Igneous Province (STLIP) magmatism to climatic and environmental perturbations during this interval. To assess the potential for massive volcanism as a trigger for marine environmental disturbances across the Smithian – Spathian boundary (SSB), the patterns and provenance of Hg sequestration in four Tethyan marine sedimentary successions are investigated in the current study. We present a diverse array of new, temporally calibrated geochemical data including Hg concentrations and isotopic compositions, strontium, and neodymium isotope records, as well as major and trace element concentrations from carbonate-poor and -rich strata alike, including volcanic ashes. Results indicate that Hg anomalies in middle to late Smithian strata vary in magnitude and age. Based on several lines of evidence, the Hg anomalies recorded for the investigated PaleoTethyan successions are interpreted to have been sourced from subduction-related arc volcanism, with potential contributions from terrestrial Hg reservoirs. In contrast, a low-magnitude mercury enrichment interval recorded for NeoTethyan late Smithian strata is attributed to hydrothermal fluid or submarine volcanic activity. These results, together with previously published Smithian to Spathian Hg records, provide evidence that Smithian Hg anomalies cannot be attributed to a singular source such as renewed STLIP activity. Instead, the stratigraphically variable mercury anomalies reflect local patterns of enhanced mercury sequestration from various sources during the middle Smithian to SSB. Consequently, evidence for STLIP magmatism during the Smithian – Spathian transition is still lacking, and regional volcanic activity may have been influential in causing marine environmental upheavals in the Tethys region across the SSB.

1. Introduction

The Early Triassic was an important interval in Earth's history, marked by the reorganization of marine and terrestrial ecosystems following the ecological devastations of the Permian-Triassic boundary mass extinction (PTBME) (Erwin et al., 2002; Hermann et al., 2012; Stanley, 2016). Studies show that biotic recovery during the Early Triassic was repeatedly interrupted by climatic, as well as marine and terrestrial environmental upheavals (e.g., Galfetti et al., 2007a; Orchard, 2007; Chen and Benton, 2012; Grasby et al., 2013a; Wei et al., 2015; Hochuli et al., 2016). The pattern of marine faunal recovery differed between nektonic and benthic organisms, with the former being characterized by a rapid Early Triassic recovery punctuated by intermittent extinctions (Orchard, 2007; Brayard and Bucher, 2015; Hautmann et al., 2015). In contrast, the main rediversification of the latter was delayed until the Middle Triassic (Foster and Sebe, 2017; Friesenbichler et al., 2021). Perhaps the most significant interval of the Early Triassic was the middle Smithian to earliest Spathian (ca. 249.9–249.1 Ma; Widmann et al., 2020). This interval was characterized by large carbon cycle perturbations (Payne et al., 2004; Galfetti et al., 2007b), significant

* Corresponding author.
E-mail address: oluwaseun.edward@unil.ch (O. Edward).

https://doi.org/10.1016/j.gloplacha.2023.104343
Received 22 September 2023; Received in revised form 17 November 2023; Accepted 11 December 2023
Available online 16 December 2023

changes in seawater temperatures (Sun et al., 2012; Romano et al., 2013), and the largest nektonic faunal extinction of the Early Triassic (Orchard, 2007; Stanley, 2009). Also, terrestrial ecosystems experienced a significant vegetation shift from lycophyte dominance in the middle Smithian to gymnosperm dominance in the early Spathian (Lindström et al., 2020 and references therein).

Causal relations between Early Triassic environmental perturbations, climatic changes and biotic turnover have been proposed and remain the subject of scientific debate (e.g., Brayard et al., 2009; Goudemand et al., 2019; Leu et al., 2019; Shen et al., 2019a; Dai et al., 2021). Notably, renewed Siberian Traps Large Igneous Province (STLIP) magmatism has been proposed as an explanation for Smithian to Spathian climatic and environmental disturbances, which have been causally related to contemporaneous biotic upheavals (Ovtcharova et al., 2006; Galfetti et al., 2007a; Payne and Kump, 2007; Sun et al., 2012; Shen et al., 2019a). However, there is currently no U-Pb zircon geochronology evidence for STLIP magmatism younger than 250.3 Ma (Augland et al., 2019; Widmann et al., 2020). Instead, mercury (Hg) enrichment intervals recorded in Smithian-Spathian marine strata from spatially disparate localities have been proposed as evidence of Smithian-Spathian transition STLIP volcanism (e.g., Grasby et al., 2016; Shen et al., 2019a).

Although generally successfully applied as a proxy for volcanism, several studies show that the biogeochemical cycling of Hg in the environment is complex and Hg anomalies can result from a variety of non-volcanic means (e.g., Grasby et al., 2019; Hammer et al., 2019; Them II et al., 2019; Shen et al., 2020; Percival et al., 2021; Yager et al., 2021). Also, the Hg content of ancient sedimentary rocks can be altered during late diagenesis (Charbonnier et al., 2020). Therefore, Hg isotopes are frequently used to constrain the provenance and trajectory of Hg deposition in both modern and ancient sediments (e.g., Rolison et al., 2013; Blum et al., 2014; Sun et al., 2014; Yin et al., 2016; Grasby et al., 2019). Unfortunately, however, of all published Early Triassic Hg records, Hg isotope data are only available for two marine sections (i.e., Chaohu, South China and Guryul Ravine, India; Wang et al., 2019a). Furthermore, the precise stratigraphic relationship between published Smithian–Spathian Hg records for different basins remains uncertain (Hammer et al., 2019; Widmann et al., 2020). Consequently, high-resolution stratigraphic correlation of Smithian to Spathian Hg records between various sedimentary basins, an assessment of the preservation of Hg contents in investigated sedimentary successions, as well as a thorough evaluation of Hg sources to Smithian to Spathian-aged marine successions, are required to reliably infer a link between Smithian Hg anomalies and a potential middle to late Smithian reemergence of STLIP volcanism.

The current study investigates the occurrence and provenance of Hg concentration anomalies in middle Smithian to Spathian sedimentary successions, with the aim of assessing the putative role of STLIP volcanism in promoting marine environmental upheavals during the studied interval. The investigated successions include carbonate-poor and carbonate-rich strata deposited in shallow and deep-water environments of the Tethys Ocean, enabling an evaluation of the intensity of Hg release to Olenekian marine depositional environments. Our dataset includes Hg concentrations and isotope compositions, carbon isotope compositions of organic matter ($\delta^{13}C_{org}$), major and trace element concentrations, mineralogical compositions, total organic carbon (TOC) content, as well as strontium and neodymium isotope ratios. Combining precise and accurate U—Pb zircon ages and conodont biostratigraphy based on unitary association zones (UAZs) (Widmann et al., 2020; Leu et al., 2022; Leu et al., 2023), a high-resolution correlation of the geochemical records from our spatially dispersed study sections is achieved. Further, we compare our Hg records to previously published Smithian to Spathian Hg records for other localities to evaluate the evidence for a singular global source for Smithian-Spathian Hg anomalies (such as renewed STLIP volcanism).

2. Geological setting

The four studied sections are currently situated in Oman and China and comprise marine sedimentary successions which were deposited in the PaleoTethys (Qiakong, Shanggang) and NeoTethys oceans (Jebel Aweri, Wadi Musjah) during the Early Triassic.

2.1. Oman

By the Early Triassic, the majority of Earth's landmass had amalgamated, forming one supercontinent – Pangea, which was bordered by a super ocean – Panthalassa (Fig. 1A). On the southern half of Pangea, the Arabian Peninsula, together with Africa and India constituted part of the Gondwana continent (Baud et al., 2001; Baud et al., 2012; Stampfli et al., 2013). Oman was situated on the northern Gondwanan margin, mainly between 20°S and 30°S and bordered to the north and east by the NeoTethys (e.g., Smith et al., 2004; Richoz et al., 2010; Brühwiler et al., 2012). The geologic evolution of the Arabian passive margin (including Oman) during the Permian to Triassic is chronicled in several studies (e.g., Baud et al., 1993; Pillevuit et al., 1997; Immenhauser et al., 1998; Baud et al., 2001; Hauser et al., 2002; Scharf et al., 2021). During the Permian, tectonic extension of the NeoTethys commenced in tandem with the northward drift of the Cimmerian Block (Şengör et al., 1984; Stampfli, 2000; Baud et al., 2012; Richoz et al., 2014), initiating the formation of offshore seamounts, which record the evolution of pelagic environments during the Triassic (Baud et al., 1993; Lapierre et al., 2004; Brosse et al., 2019). Afterwards in the Jurassic, the Triassic offshore seamounts and other Permian-Triassic rocks were redeposited (via tectonism-driven submarine gravity sliding) within Jurassic sediments as olistostromes, which can be found in both the Hawasina Basin and Batain plain of Oman (Pillevuit et al., 1997; Schreurs and Immenhauser, 1999).

The Jebel Aweri (JA) outcrop (22.3556666667° N, 59.7541944444° E) is an exotic build-up block located in the Batain plain, northeastern Oman (Fig. 1E). Details of the geologic evolution of the Batain plains have been discussed in different studies (e.g., Immenhauser et al., 1998; Schreurs and Immenhauser, 1999; Hauser et al., 2002). The JA carbonate succession is situated about 30 km south of Ras al Hadd, Oman. It is located alongside successions of the Middle Jurassic Guwayza Formation and the Ad Daffah conglomerate in the Batain area. This exotic block comprises a 22 m-thick lower block and an 8 m-thick upper block and represents a Lower Triassic reefal succession consisting of shell-supported biostrome, cemented lime clasts and microbialite bioherm (dendrolitic stromatolite) of late Smithian to Spathian age (Leu et al., 2023). Thus, the JA exotic block constitutes an Early Triassic offshore seamount carbonate succession, which has been redeposited as an olistostrome within Jurassic sediments (Schreurs and Immenhauser, 1999; Brosse et al., 2019).

The Wadi Musjah (WMJ) outcrop (22.9623611111° N, 58.2670555556° E) is a 4.6 m-thick, strongly condensed, red ammonoid limestone succession located about 75 km from Muscat, Oman (Fig. 1E). This succession was previously described by Baud et al. (2001), Brühwiler et al. (2012), and most recently by Leu et al. (2023). The WMJ section comprises Hallstatt-type limestones, which are pelagic carbonate deposits with near zero terrigenous components and are known from several other Tethyan localities (Brühwiler et al., 2012). These Hallstatt-type limestones from the Arabian margin have been interpreted to represent isolated oceanic build-ups i.e., seamounts, which have been transported on the Arabian margin during the Late Cretaceous obduction of oceanic crust (Brühwiler et al., 2012; Baud, 2013). Based on conodont biochronology, the WMJ succession covers the middle Smithian to Spathian (Leu et al., 2023). Thus, WMJ spans a longer time interval than the six-times thicker JA build up block, albeit having a lower (ca. 6× lower than JA) sedimentation rate. The lower 2.4 m of the succession consists of cemented bivalve coquina biostromes and peloidal grainstone with centimeter-sized bivalves in fibrous and blocky calcite

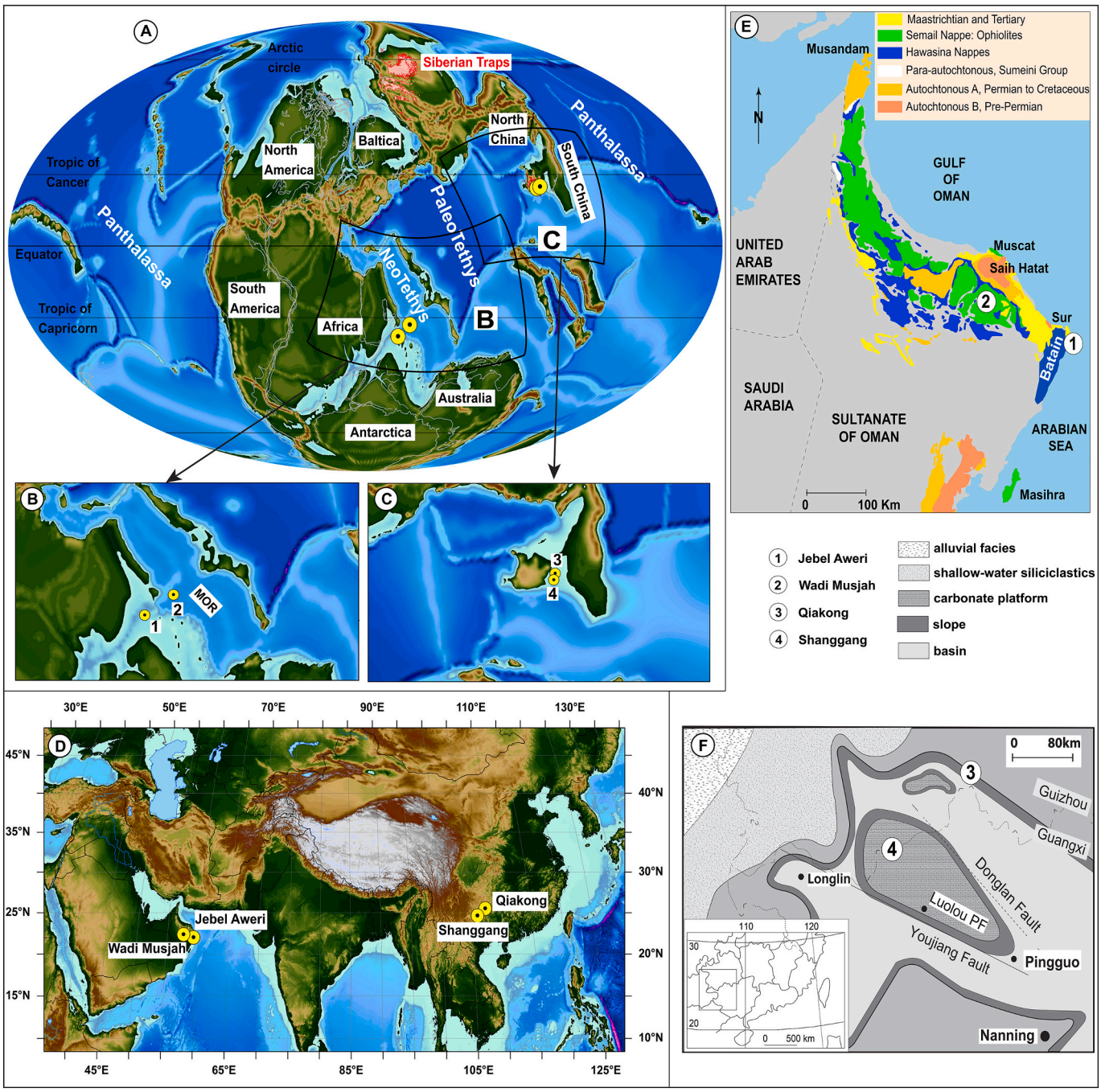

Fig. 1. Paleogeographic, present-day and geologic maps of the study locations. A) Early Triassic paleogeographic map after the Panalesis model (Vérard, 2019) showing the location of the studied successions in the PaleoTethys and NeoTethys. Mollweide projection of the B) Oman (NeoTethys) and C) South China (PaleoTethys) areas during the Early Triassic from A. D) Map showing the present-day location of the studied successions. Geological map of E) Oman with the present-day locations of the exotic blocks modified after Baud et al. (2001), and F) the Nanpanjiang basin after Bagherpour et al. (2017) showing the studied sections. MOR: mid-oceanic ridge.

cement. The upper 2.2 m of the section is characterized by a sudden appearance of crinoid ossicles, brachiopod shells, and echinoid spines, which form yellow to brown colored calcite cemented encrinites-brachiopod biostromes (Leu et al., 2023).

2.2. South China

The South China Block was situated along the eastern margin of the PaleoTethys ocean and occupied equatorial to intertropical paleolatitudes in the Early Triassic (Fig. 1A). The studied sections in South China are situated in the Nanpanjiang Basin, which is in the present-day southern section of the South China block (southern Guizhou and northwestern Guanxi provinces; (Enos et al., 2006)). During the Late Permian to Early Triassic, the Nanpanjiang Basin developed as an extensional to transtensional basin in a back-arc setting (Duan et al., 2020). Rock successions of this basin extend across southern China and northern Vietnam (Leu et al., 2022 and references therein) and include Early Triassic sedimentary deposits representing deep-water, slope/basinal settings and isolated shallow-water carbonate platforms (Lehrmann et al., 2007; Duan et al., 2020). The Nanpanjiang Basin is

characterized by a fault-bounded (graben and horst) paleotopography (Bagherpour et al., 2020), with horsts consisting of carbonate platforms (such as the Great Bank of Guizhou (GBG) and Luolou platform (Lehrmann et al., 1998; Bagherpour et al., 2017)) and the grabens consisting of distal turbidites and slope to basin deposits (such as the Pingtang syncline (Bagherpour et al., 2020; Widmann et al., 2020)).

The Qiakong (QIA) section (25.8573277778° N, 107.3089138889° E) is situated in the Pingtang syncline, northern Nanpanjiang Basin and consists of Early Triassic sediments of the Daye and Luolou formations. The Smithian to Spathian succession in QIA comprises middle Smithian thin-bedded limestone strata with volcanic ashes of the Daye Formation (Widmann et al., 2020; Leu et al., 2022). These are overlain by alternating beds of laminated black shale and thin-bedded limestone of late Smithian age, which accumulated in a slope/basin setting (Leu et al., 2022). The Spathian portion of the Luolou Formation in QIA was deposited in an outer platform setting (Galfetti et al., 2007a; Leu et al., 2022). It comprises conodont- and ammonoid-rich nodular limestone and marly limestone beds, as well as interbedded volcanic ash beds.

The Shanggang (SHA) succession (24.812333° N, 106.542194° N) is situated in the northern part of the Guangxi province, China and was deposited on the laterally extensive Luolou platform of the Nanpanjiang Basin (Fig. 1F). It consists of mixed siliciclastic and carbonate deposits in the Smithian interval and nodular limestone beds in the Spathian (Widmann et al., 2020; Leu et al., 2022). Several volcanic ash beds are intercalated within the Smithian-Spathian succession, which is subdivided into several lithological units ranging from the early Smithian thin-bedded "*Flemingites*" limestone of Unit III to the Spathian cliff-forming nodular limestone beds of unit V (Galfetti et al., 2008; Leu et al., 2022).

3. Materials and methods

Materials analyzed for this study – whole rock carbonates, shales, volcanic ashes, as well as fossil conodont and fish teeth samples – are from recent studies of the Nanpanjiang Basin (Widmann et al., 2020; Leu et al., 2022) and Oman exotic blocks (Leu et al., 2023). These recent studies provided detailed sedimentological descriptions and carbon isotope chemostratigraphy for the study sites. Furthermore, U—Pb zircon geochronology and conodont biochronology from these recent studies provide the correlation framework and absolute time constraint utilized in the current study. Whole rock samples from each of the localities were analyzed for Hg concentration and isotope composition, total organic carbon (TOC) content, major element, and trace element concentration, respectively. Conodont elements and fossil fish teeth fragments from the Oman study sites (Leu et al., 2023) were analyzed for their Sr and Nd isotope compositions and volcanic ash samples from QIA and SHA were analyzed for their major and trace element concentrations, as well as Hg concentration and isotope compositions.

3.1. Mercury concentration and isotope composition

Mercury content of pulverized shales, carbonates and volcanic ashes was measured at the Institute of Earth Sciences (ISTE), University of Lausanne (UNIL) using a Zeeman R-915F high-frequency atomic absorption spectrometer. Analyses were made in duplicate for all samples. For the samples with outlier Hg concentrations in each of the studied sections, three extra measurements were done to ensure both the representativeness and analytical precision for the sample. The standard reference material – GSD-11 (Chinese alluvium) – was used to monitor accuracy of the measurements.

Hg isotope analyses were made at the Observatoire Midi-Pyrénées, Toulouse, France, following analytical procedures reported in Sun et al. (2013) and Jiskra et al. (2021). Briefly, Hg was preconcentrated as Hg^{II} from pulverized samples using the double-stage furnace – acid-trapping technique (Sun et al., 2013). Two reference materials, NIST SRM 1632D (bituminous coal, $n = 5$) and NIST SRM 1944 (New Jersey sediment, $n = 4$), were processed along with the samples. This was followed by Hg isotope analysis by cold vapor multi-collector inductively coupled plasma mass spectrometry (CV-MC-ICPMS). Measurements were carried out in duplicates over two analytical sessions following previously documented analytical procedures (Sonke et al., 2010; Jiskra et al., 2021). Sample-standard bracketing (Blum and Bergquist, 2007) using the NIST SRM 3133 standard at matching standard and sample concentrations (1 and 2.1 ng/g) was used to correct the MC-ICPMS instrumental mass bias. Repeated analysis of the UM-Almaden ($n = 14$) and ETH-Fluka (n = 14) Hg standard solutions at matching sample concentrations were used to monitor long term instrumental precision.

Hg isotope compositions are reported as the mean of duplicate measurements using the delta notation (δ) in permil (‰) relative to the bracketing NIST SRM 3133 standard (Blum and Bergquist, 2007). For mass dependent fractionation (MDF), this is expressed as $\delta^{202}Hg$ in permil (‰) and for mass independent fractionation (MIF), values as reported using the capital delta (Δ) notation:

$$\Delta^{xxx}Hg = \delta^{xxx}Hg - K_{xxx} \times \delta^{202}Hg \quad (1)$$

where xxx refers to Hg isotope mass, except ^{198}Hg, and K represents the mass-dependent scaling factor for the different Hg isotope masses. We report analytical uncertainty of Hg isotope values conservatively by using whichever is larger between the 2 × standard deviation (2σ) of the replicate measurements or that of the certified reference material with the largest 2σ.

3.2. Total organic carbon (TOC) content and carbon isotope analysis

TOC was measured at ISTE using two analytical methods: (i) Rock-Eval pyrolysis of bulk (non-decarbonated) sample material and (ii) TOC determination on decarbonated samples using an Elemental Analyzer. A Rock-Eval 6 was used to measure TOC content in volcanic ashes and a subset of limestone and shale samples following the procedure described by Behar et al. (2001). The standard – IFP-160000 was used to monitor analytical quality and analytical error was <0.1%. Pulverized material from the remainder subset of shale and limestone samples was decarbonated by acid treatment overnight using 3 M HCl. The residues were then rinsed several times with deionized water and dried in an oven at 45 °C for three days. TOC content and carbon isotope compositions ($\delta^{13}C_{org}$) were measured on the acid treated samples using a Carlo Erba (1100 CE) Elemental Analyzer linked to a Thermo Fisher Delta V Plus isotope ratio mass spectrometer. $\delta^{13}C_{org}$ values were measured only for samples from QIA and SHA because the samples from the Oman exotics have too low organic matter (OM) contents. The internal standards: glycine, pyridene, urea and graphite used for $\delta^{13}C_{org}$ analysis are calibrated against IAEA standards: USGS-24 graphite ($\delta^{13}C = -15.9$ ‰) and NBS-22 oil ($\delta^{13}C = -29.7$ ‰) (Spangenberg and Herlec, 2006). Final TOC contents were calculated from the EA TOC yields and documented weights of the samples before and after acid treatment.

3.3. Major and Trace elements analysis

Major element (ME) and trace element (TE) concentrations were determined by X-ray fluorescence (XRF) spectrometry using a PANalytical Axios^{mAX} wavelength dispersive XRF spectrometer fitted with a 4.0 kW Rh X-ray tube at ISTE, UNIL. For ME analysis, about 1.2 g of calcined sample powder was mixed with 6 g of lithium tetraborate ($Li_2B_4O_7$) and heated to 1250 °C to make fused disks prior to analysis. For TE, measurements were conducted on pressed disks obtained by pressing a homogenized mixture of 12 g of sample powder and 3 g of Hoechst-C-wax. The detection limits are approximately 0.01% for MEs and 1 to 7 ppm for TEs. The external reproducibility (1σ) varies between 0.5 and 5% depending on the element. The accuracy of analyses was assessed using standard reference materials: JLS-1, JDO-1 and BHVO.

3.4. Strontium and Neodymium isotopes

Radiogenic isotope ratios of Sr ($^{87}Sr/^{86}Sr$) and Nd ($^{143}Nd/^{144}Nd$) in bioapatite material (conodont elements and fish teeth) from the Omani sections were measured at the Department of Earth Sciences, University of Geneva, Switzerland. Bioapatite samples were dissolved in a few drops of concentrated HNO_3 (16 N) over night and brought to evaporation over a hot plate at 80 °C. Samples were re-dissolved in 1 N HNO_3 and a sequential chromatographic column was used to separate Sr and Nd. Sr separation was done using Eichrom Sr Spec resin in a solution of 1 N HNO_3 (Pin and Bassin, 1992). Neodymium was separated using two ion chromatography columns. Eichrom TRU-Spec™ resin (in solution of 1 N HNO_3) was used during the first extraction step to remove the Rare Earth Elements (REE) from the initial solution while the Eichrom LnSpec™ resin (in solution of 0.25 N HCl) was used during the second step to separate Nd from other REE (Caro et al., 2006). The total procedural Nd blanks were smaller than 5 pg and thus is negligible compared to the Nd content of samples (> 200 ng). Nd and Sr isotope ratios were measured on a Neptune MC-ICP-MS (Thermo Finnigan) using an Apex Omega injection system. Nd isotope values were corrected for internal fractionation using $^{146}Nd/^{144}Nd = 0.7219$ and for external fractionation by multiple analyses ($n = 26$) of JNdi-1 standard at 25 ppb concentration ($^{143}Nd/^{144}Nd = 0.512115$, Tanaka et al. (2000); $2\sigma = 1.6 \times 10^{-5}$). The Rb content of the Sr purified samples was small ($^{85}Rb/^{86}Sr < 0.1$ ‰) and thus, no Rb correction was applied to Sr measurements on the MC-ICP-MS. Kr interference was monitored by measurements of the $^{83}Kr/^{86}Kr$ and $^{83}Kr/^{84}Kr$ ratios. The accuracy and reproducibility of the Sr isotope measurements were checked with the NBS SRM 987 standard ($^{87}Sr/^{86}Sr = 0.710248$, McArthur et al. (2001); $2\sigma = 4.4 \times 10^{-6}$; $n = 25$). The Nd isotope values ($^{143}Nd/^{144}Nd_{(0)}$) were corrected for radiogenic production of ^{143}Nd (Martin and Macdougall, 1995) and expressed as $\varepsilon_{Nd(t)}$ (see supplementary information).

3.5. Bulk rock mineralogical composition

Representative samples from both the Oman and South China successions were selected for analysis of their bulk rock mineralogy using X-ray diffraction (XRD) spectrometry. XRD analysis was conducted using a Thermo Scientific™ ARL™ X'TRA diffractometer fitted with a copper tube operating at 30 mA and 40 kV at ISTE following the procedure outlined in Adatte et al. (1996). Homogenous powdered samples, obtained by milling whole rocks (particle sizes <40 μm), were pressed into a powder holder by using a glass slide and subsequently scanned from 2° to 65° two-theta in steps of 0.02° two theta using a one second per step counting time. Bulk mineralogy was determined semi-quantitatively based on XRD peak intensities of the main minerals relative to external standards (Kübler, 1983; Adatte et al., 1996). Uncertainty for grain minerals was about 5 wt% and 5–10 wt% for phyllosilicates.

4. Results

All the geochemical data generated for this study are provided in the supplementary files hosted on Mendeley data (Edward et al., 2023a) and are illustrated in Figs. 2 to 6.

4.1. Mercury content and isotope composition

Hg concentrations have a range between 1 and 216 ppb, < lower level of detection (LLD) to 126 ppb, < LLD to 21 ppb and < LLD to 4 ppb for SHA, QIA, JA and WMJ, respectively. Background Hg contents are higher for South China (< 10 ppb) than for Oman successions (< 1 ppb; LLD). Except for the WMJ succession, Hg concentration anomalies (and Hg/TOC for samples with TOC > 0.2 wt%) are recorded within the Smithian interval in all localities, albeit with different stratigraphic extent and magnitude. For QIA, a Hg anomaly is recorded for the upper middle Smithian to the latest Smithian (Fig. 2). The Smithian Hg anomaly for SHA appears to be pulsed, with an initial minor peak in the lower middle Smithian and a main peak recorded between the upper middle Smithian to latest Smithian (Fig. 2). For JA, a low-magnitude Hg anomaly is recorded and is restricted to the upper late Smithian (Fig. 3A).

Hg isotope MDF ($\delta^{202}Hg$) values are generally higher for QIA (range: −2.5 to −0.58 ‰) compared to SHA (range: −2.78 to −1.26 ‰). In this study, we focus on Hg MIF values as these are more diagnostic of the sources and depositional pathways of Hg in the natural environment (Blum et al., 2014; Yin et al., 2014; Yager et al., 2021) and have been shown to be resistant towards post-depositional alteration (Chen et al., 2022). For QIA, $\Delta^{199}Hg$ and $\Delta^{200}Hg$ values are near zero (0 ± 0.05 ‰), with a median value of 0.01 ‰ and 0.00 ‰, respectively. Hg MIF values have a range between −0.05 ± 0.1 ‰ – 0.06 ± 0.1 ‰ and 0.04 ± 0.07 ‰ to −0.06 ± 0.07 ‰ for $\Delta^{199}Hg$ and $\Delta^{200}Hg$, respectively. SHA samples have slightly positive $\Delta^{199}Hg$ values (range: 0.01 ± 0.1 ‰ to 0.16 ± 0.1 ‰, median: 0.07 ‰), except for 1 volcanic ash sample (−0.25 ± 0.1 ‰) and 2 limestone samples (−0.11 ± 0.1 ‰ and − 0.07 ± 0.1 ‰, respectively). Similar to QIA, $\Delta^{200}Hg$ values for SHA are near zero (median: 0.02 ‰), except for 1 limestone and volcanic ash sample that have slightly negative values (−0.07 ± 0.07 ‰). Secondary reference materials analyzed to monitor the external reproducibility of the Hg isotope measurements (NIST SRM 1632D and NIST SRM 1944) have Hg isotope MIF values (Table S6) consistent with those previously published for these materials (Sonke et al., 2010; Sun et al., 2013; Jiskra et al., 2019).

4.2. TOC contents and $\delta^{13}C_{org}$

TOC contents are higher for South China than Oman. All samples for both Oman successions have TOC content <0.1 wt%, except for sample C15 in JA with 0.16 wt% TOC (Fig. 3). For South China, volcanic ash and limestone samples generally have TOC contents <0.2 wt%, except some samples within the late Smithian Hg enrichment interval and one early Smithian sample in SHA (Fig. 2). TOC content differs between different lithologies, as samples with TOC content >0.2 wt% for SHA are predominantly dark mudstone or shale samples (Fig. 2B). No systematic difference in TOC content based on analytical technique (i.e., Rock-Eval vs. Elemental Analyzer, Fig. 2) is observed.

$\delta^{13}C_{org}$ values have a range from −31.8 ‰ to −26.2 ‰ for QIA and − 30.1 ‰ and − 25.7 ‰ for SHA. Both localities are characterized by a negative $\delta^{13}C_{org}$ excursion in the middle Smithian, which is succeeded by a late Smithian positive excursion, which peaks in the earliest Spathian (Fig. 2). This organic carbon $\delta^{13}C$ trend is similar to that of inorganic carbon $\delta^{13}C$, which was previously reported for these sections by Widmann et al. (2020) and Leu et al. (2022).

4.3. Major and Trace element concentration

In addition to OM, Hg sequestration can be influenced by the terrigenous input, as well as marine redox conditions (Grasby et al., 2019; Shen et al., 2020; Them II et al., 2019). Al, Fe, Mo and U contents are commonly evaluated together with Hg to assess whether variations in clay content, precipitation of pyrite or Fe (oxy) hydroxides resulting from marine redox changes is the main control on Hg sequestration (e.g., Charbonnier et al., 2017; Wang et al., 2019a; Shen et al., 2020). Spearman's rank correlation analysis is used to assess the strength (ρ) and significance (p) of potential statistical correlations between Hg and Al, Fe, Mo, and U contents in the studied sections. Spearman's rank correlation analysis is advantageous because it can be used to evaluate the statistical correlation between two variables which do not necessarily have a linear relationship (e.g., Vickers et al., 2023). Al content (Al_2O_3) is higher for South China (max: 28 wt%) than for Oman (max: 3 wt%) and varies according to lithology (Fig. S1) as follows: volcanic ashes > shales > carbonates. Al shows no statistical correlation to Hg in the studied sections, except for SHA samples which show a moderate but significant correlation ($\rho = 0.50$, $p = 0.03$). Fe_2O_3 concentrations range

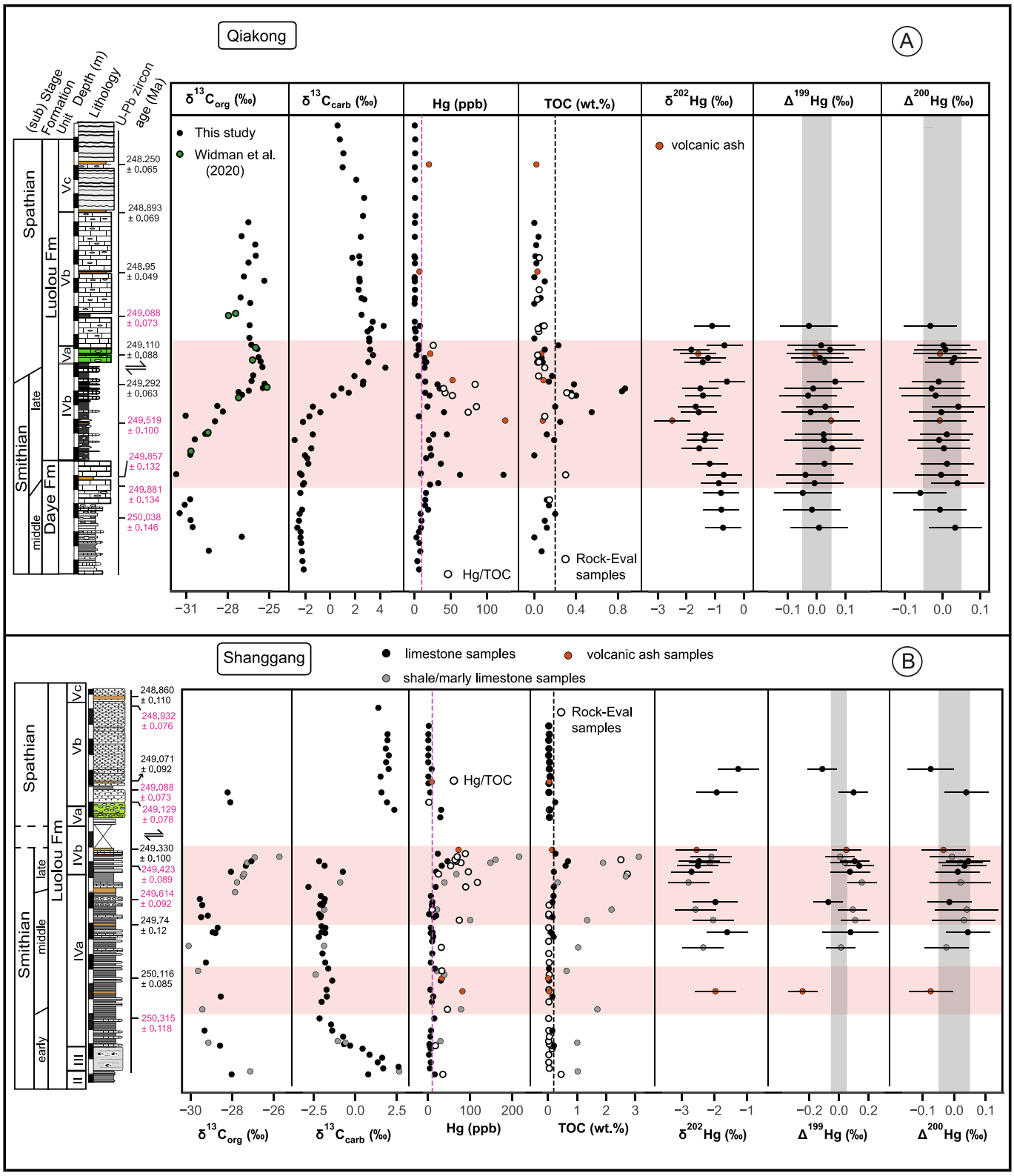

Fig. 2. Geochemical profiles showing carbon isotope ($\delta^{13}C$), mercury (Hg) concentration and Hg/TOC ratios, TOC contents, Hg isotope mass-dependent fractionation (MDF, $\delta^{202}Hg$), and Hg isotope mass-independent fractionation (MIF) records ($\Delta^{199}Hg$, $\Delta^{200}Hg$) from A) Qiakong and B) Shanggang sections. $\delta^{13}C_{carb}$ data and U-Pb zircon ages are from Widmann et al. (2020). Absolute ages in pink colour are derived by Bayesian age-depth modeling (Widmann et al., 2020). Dashed vertical black line on TOC plot depicts 0.2 wt% TOC limit and pink vertical dashed line on Hg, Hg/TOC profiles represent background Hg contents (10 ppb). Horizontal pink bands depict the intervals of Hg enrichment. Vertical gray bands on the Hg MIF records depicts the interval of near zero Hg isotope MIF (0 ± 0.05 ‰). (For interpretation of the references to colour in this figure legend, the reader is referred to the web version of this article.)

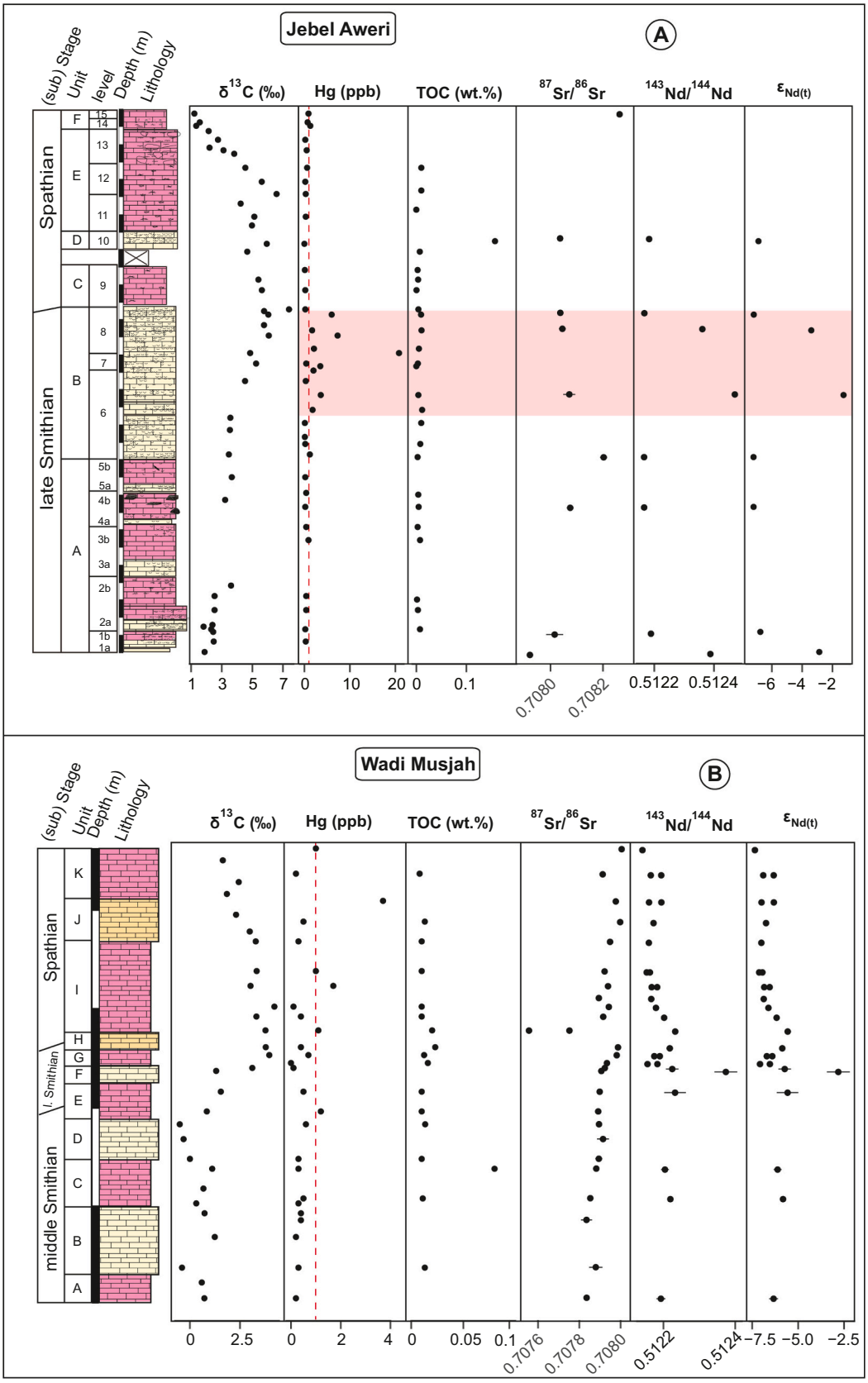

Fig. 3. Carbon isotope ($\delta^{13}C_{carb}$), mercury concentration, TOC content, strontium isotope and neodymium isotope records for A) Jebel Aweri and B) Wadi Musjah. $\delta^{13}C$ values are from Leu et al. (2023).

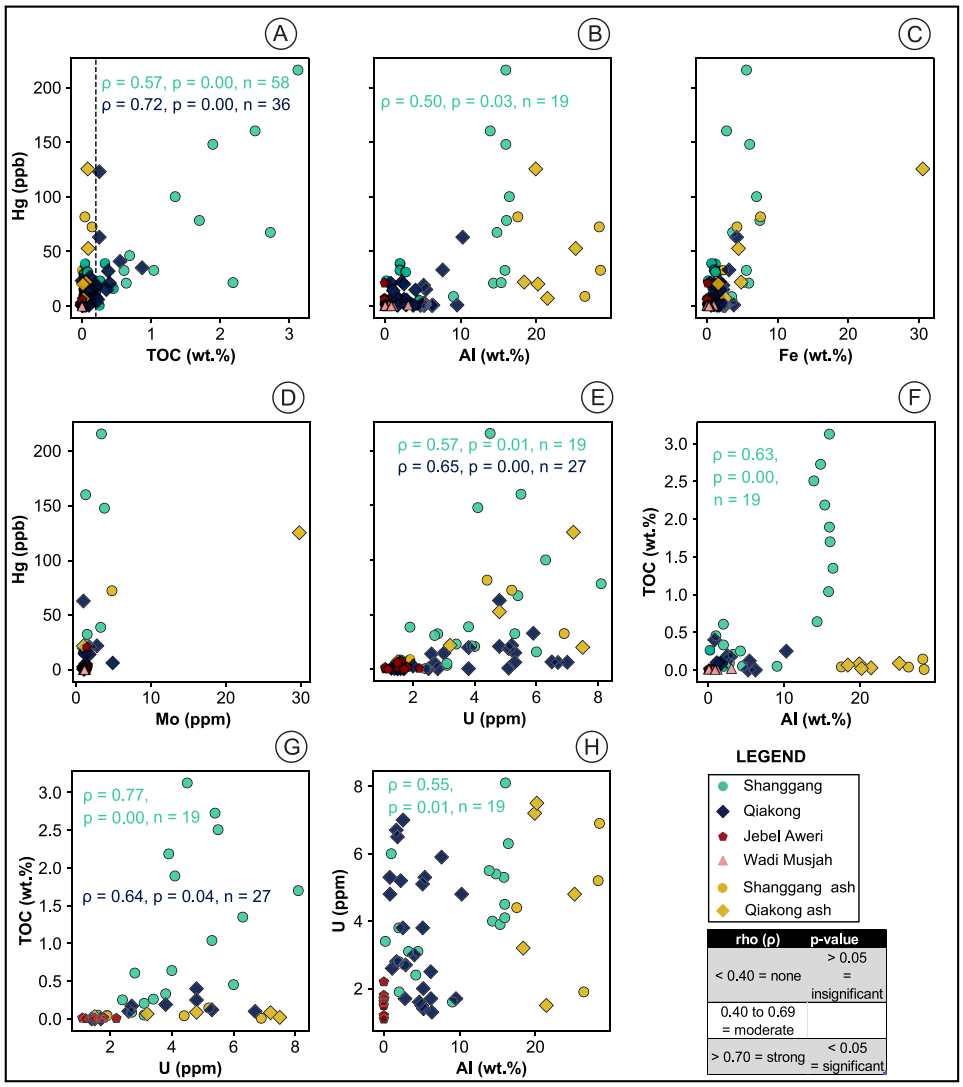

Fig. 4. Cross plots showing the statistical relationship between mercury (Hg) and A) TOC. Black line represents the suggested 0.2 wt% TOC limit for Hg/TOC normalization (Grasby et al., 2016), B) Al, C) Fe, D) Mo, E) U. Cross plots of F) TOC vs. Al, G) TOC vs. U, H) U vs Al. Spearman's correlation coefficient (ρ) and *p*-values (p) are given within individual cross plots only when a significant correlation is observed (i.e., p-value <0.05). Volcanic ash samples were not included in the calculation of correlation coefficients.

between 0.02 wt% and 30.54 wt%. Like Al, the highest Fe contents are measured in volcanic ashes. However, there is no correlation between Fe and Hg in any of the studied sections (Fig. 4). Mo contents are very low for all samples and have a range between <1 ppm (i.e., below lower limit of detection (LLD) of the XRF spectrometer) and 5 ppm, except for sample Q3T with 30 ppm. Like Fe, Mo has no statistically significant correlation to Hg in any of the studied sections (Fig. 4). U contents range between 1 and 8 ppm for QIA and SHA but is much lower for JA (range = 1–2 ppm) and WMJ (< LLD) (Fig. S1). A moderate but significant correlation is recorded between Hg and U for both SHA and QIA but is absent for JA and WMJ.

Volcanic ash samples have high LOI values (7.4 ≤ LOI ≤ 23.1 wt%), similar to other Permian-Triassic volcanic ashes from South China (e.g., He et al., 2014; Wang et al., 2019b; Edward et al., 2023b). LOI-corrected SiO_2, Al_2O_3 and total alkali ($Na_2O + K_2O$) concentrations have a range between 38.6 and 67.9 wt%, 17.5 and 28.4 wt%, and 3.0 and 9.0 wt%, respectively. TiO_2/Al_2O_3 ratios for all volcanic ash samples are generally <0.055 (Table S5), suggesting that the ashes retain primary geochemical compositions (Hong et al., 2019). Nevertheless, only immobile elements, which are less susceptible to post-depositional alteration (Hong et al., 2019; Portnyagin et al., 2020), are utilized for subsequent interpretation of the tectonic provenance of the volcanic ashes. Primitive mantle-normalized trace element patterns (Sun and McDonough, 1989) indicate that ashes are characterized by conspicuous Ta, Nb, Sr and Ti negative anomalies (Fig. 5A, 5B), consistent with a subduction-related tectonic provenance (Pearce et al., 1995).

4.4. Strontium and Neodymium isotopes

Smithian to Spathian $^{87}Sr/^{86}Sr$ values for WMJ and JA fall within the global Olenekian range of $^{87}Sr/^{86}Sr$ values (i.e., 0.70759–0.70848, Martin and Macdougall, 1995; Sedlacek et al., 2014; Song et al., 2015). Values are generally lower for WMJ (0.707556 ± 6.0 × 10^{-6} to 0.708005 ± 7.1 × 10^{-6}) than JA (0.707922 ± 1.2 × 10^{-5} to 0.708202 ± 1.3 × 10^{-5}). For both JA and WMJ, $^{87}Sr/^{86}Sr$ values are generally characterized by an increasing trend between the Smithian and Spathian (from 0.707835 ± 5.0 × 10^{-6} to 0.708005 ± 7.1 × 10^{-6}). However, this trend is punctuated by slightly lower values around the Smithian – Spathian boundary (SSB; Fig. 3). For WMJ, $\varepsilon_{Nd(t)}$ values are between −7.5 ± 0 and − 5.7 ± 0.6 except sample WMJ 1 which has a value of −3.0 ± 0.6. $\varepsilon_{Nd(t)}$ values for JA have a range between −7.0 ± 0.1 and − 1.1 ± 0.1, with the highest values recorded in the latest Smithian

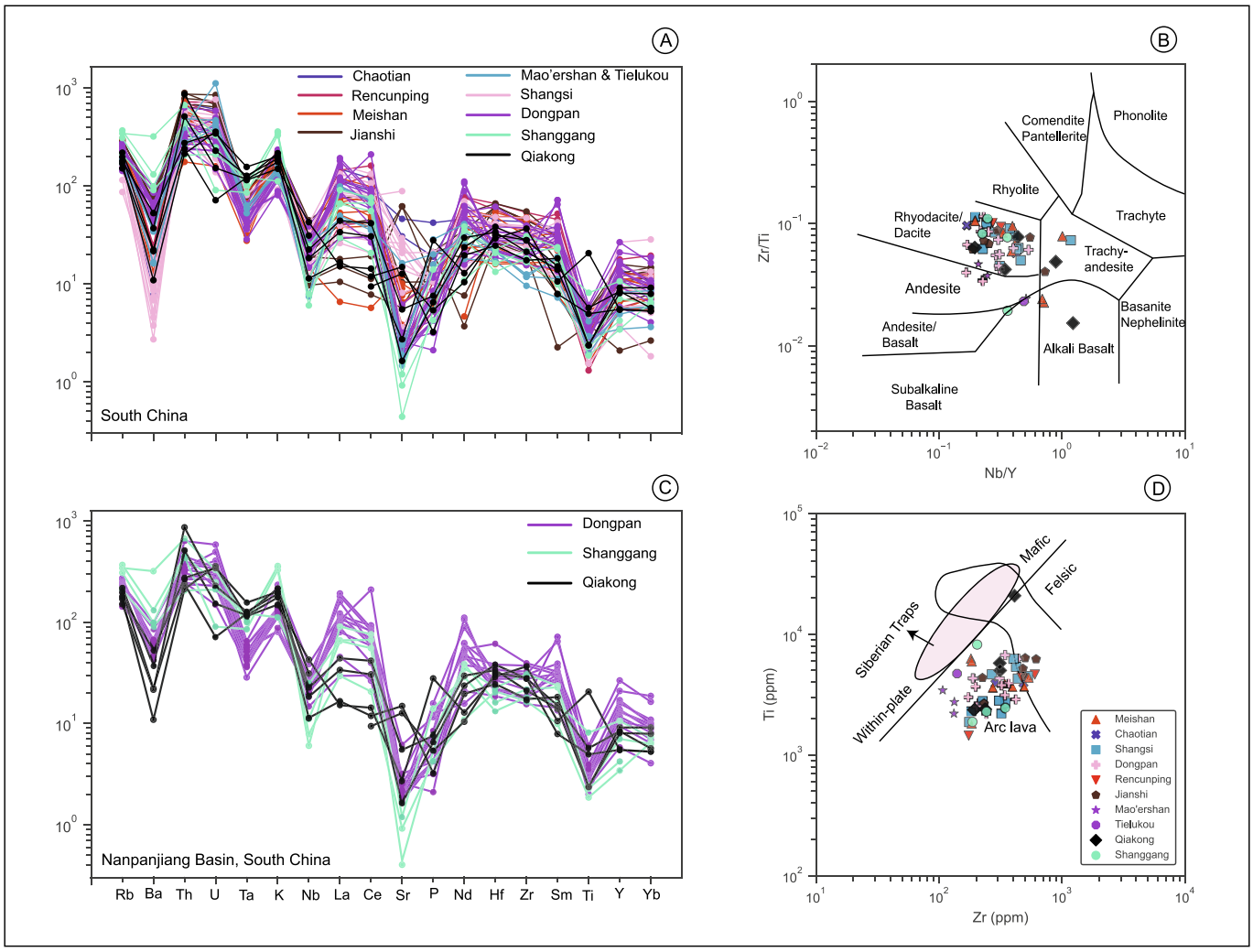

Fig. 5. Major element and trace element composition of volcanic ash samples from Qiakong and Shanggang. A, B) Primitive mantle-normalized spider diagram comparing incompatible trace element concentrations for Olenekian (Smithian and Spathian) volcanic ashes from the studied sections compared with Changhsingian to Induan volcanic ashes from other localities in South China. Data for other sections in South China are from (He et al., 2014; Wang et al., 2019b; Zhao et al., 2021; Song et al., 2022). Primitive mantle normalization values are from (Sun and McDonough, 1989). C) Zr/Ti vs Nb/Y classification diagram (Winchester and Floyd, 1977) for volcanic ashes from the Nanpanjiang Basin and other localities in South China. D) Ti vs Zr tectonic setting classification diagram (Pearce, 1982) for the volcanic ash samples from the current study compared with other volcanic ash samples from South China. The field labelled Siberian Traps in D) is after He et al. (2014).

(Fig. 3). Notably, both WMJ and JA record an increase in $\varepsilon_{Nd(t)}$ values in the latest Smithian, which for JA coincides with decreasing $^{87}Sr/^{86}Sr$ values (Fig. 3A).

4.5. Mineralogical compositions

XRD analyses indicate that QIA samples are predominantly composed of calcite, phyllosilicates, quartz, and plagioclase feldspar, with average proportions of 66%, 16%, 12%, and 4%, respectively. Rare occurrences of minerals such as pyrite, dolomite and ankerite are also recorded (Fig. 6). The mineralogical composition of QIA samples is consistent with the mixed carbonate and siliciclastic lithological make-up of this section. In contrast with QIA, samples from the Oman exotics contain about 95% calcite. For JA, samples comprise on average 98% calcite and variable proportions of quartz and phyllosilicates. WMJ samples contain, on average, 94% calcite and variable proportions of quartz and phyllosilicates.

5. Discussion

5.1. Assessing the preservation of the $\delta^{13}C$ and Hg records

The preservation of the rock successions in the studied sections are evaluated to assess the reliability of their Hg and $\delta^{13}C$ records. TOC measurements indicate that the majority of analyzed material is characterized by low OM content (section 4.2). Low TOC contents may be due to primary limited burial of organic matter in the sediments or may have resulted from post-depositional oxidation of OM in these successions. The Oman exotic block successions (i.e., WMJ and JA) were probably characterized by very limited initial terrestrial OM content owing to their offshore paleo-depositional environment. Hence, any OM in these successions would probably have been marine. For the Nanpanjiang Basin sections – QIA and SHA, the source and preservation of OM can be evaluated using the Rock-Eval pyrolysis data. Analyzed samples with high OM content plot within the field of kerogen type III, corresponding to a terrestrial OM source (Espitalié et al., 1985). However, the high T_{max} values for most samples ($n = 49/66$) suggests that OI and HI values have been altered by burial diagenesis (Fig. 7B),

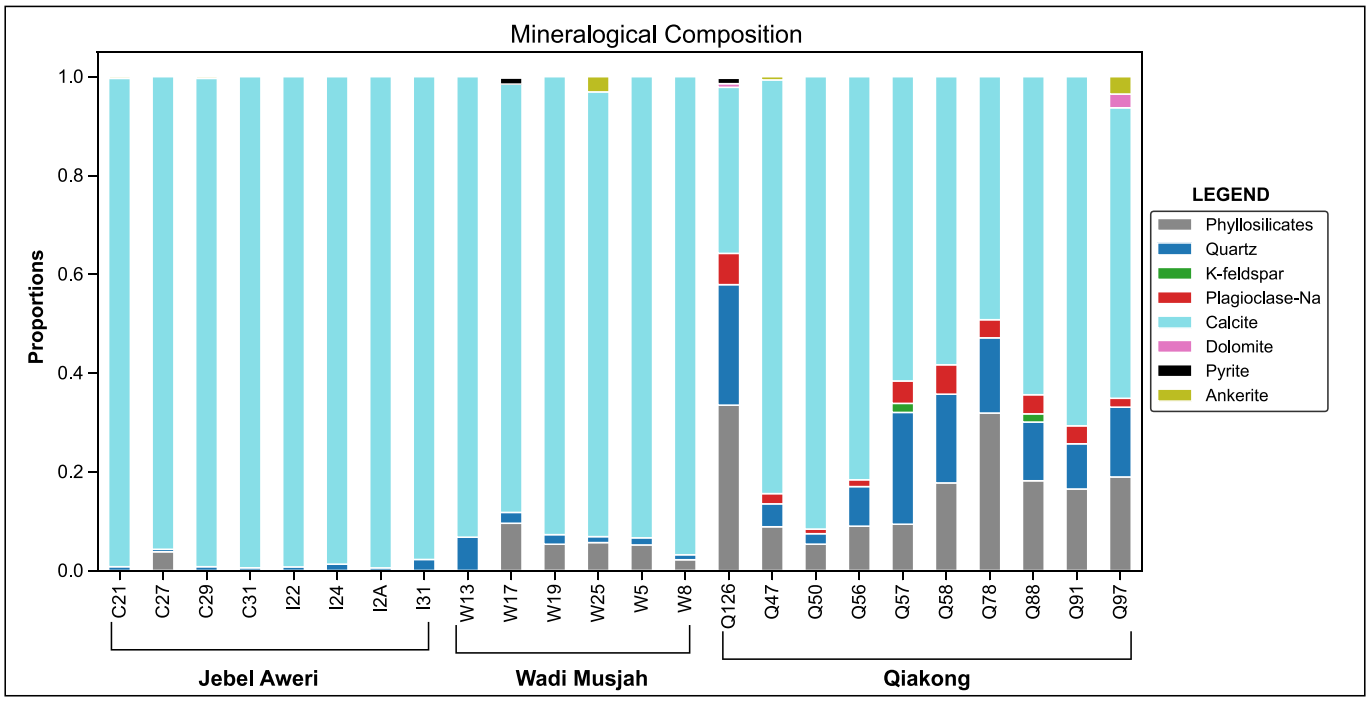

Fig. 6. Semi-quantitative estimation of the main mineral constituents of rock samples from the studied successions in Jebel Aweri and Wadi Musjah (Oman) and Qiakong (South China).

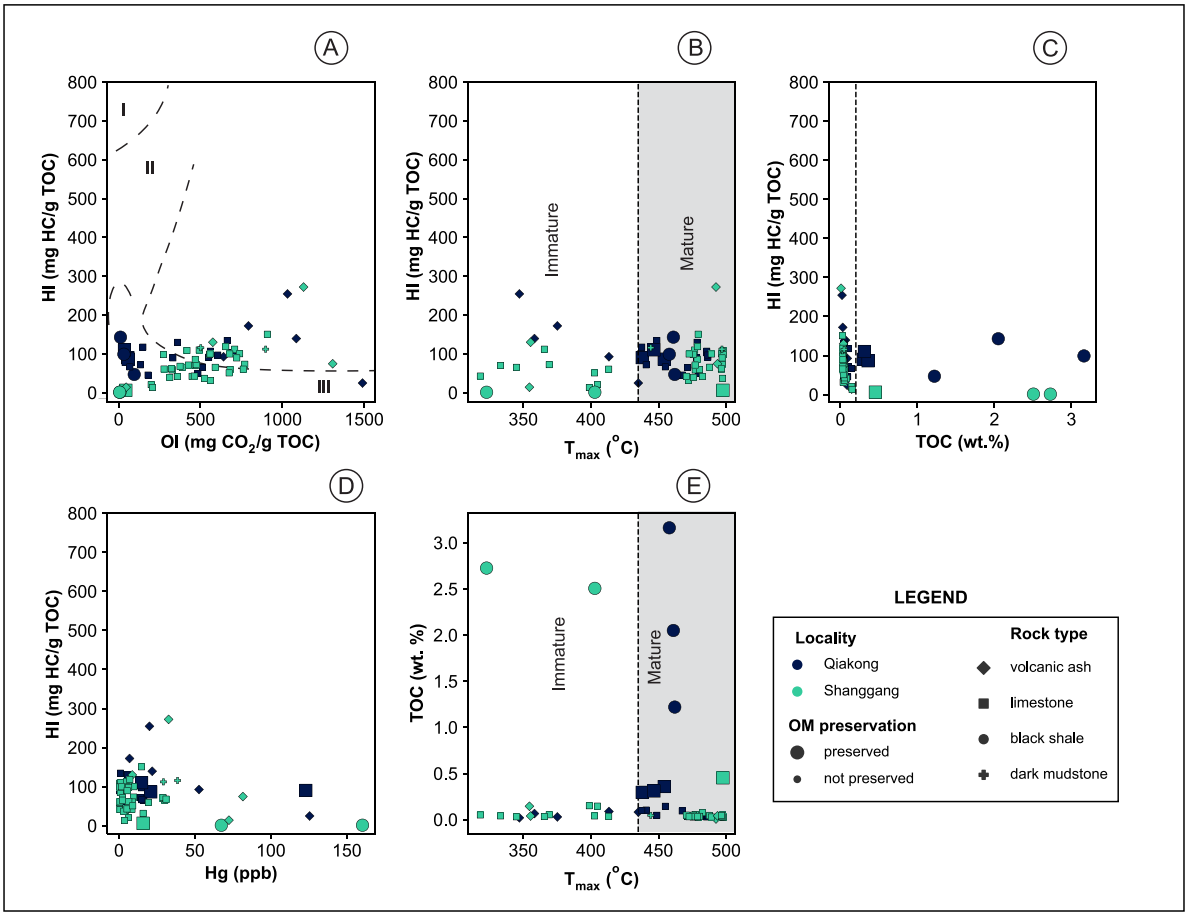

Fig. 7. Scatterplot of Rock-Eval pyrolysis data for Qiakong and Shanggang. A) HI vs. OI, B) HI vs. T_{max}, C) HI vs. TOC. Dashed black line denotes the 0.2 wt% TOC preservation limit (Grasby et al., 2016), D) HI vs. Hg, E) TOC vs. T_{max}. Samples interpreted to have preserved organic matter have TOC > 0.2 wt%. OM = organic matter.

complicating the interpretation of OM source for these successions based on these values only. Nevertheless, the low HI values for samples with >0.2 wt% TOC (Fig. 7) may indicate that SHA and QIA are predominantly characterized by terrestrial OM, a mixture of terrestrial and oxidized marine OM or that these successions comprise completely reworked OM (Espitalié et al., 1985; Fantasia et al., 2018). Terrestrial OM contribution to the South China sections is supported by the presence of woody particles in QIA (Widmann et al., 2020). Also, the moderate but significant correlation between TOC and Al for SHA (Fig. 4F) supports terrestrial OM contribution to this succession. However, this correlation can also be explained by lithology (e.g., mudstone yielding higher TOC values). Thus, a dominant OM source for these successions cannot be confidently inferred.

Despite the poor preservation (or lack) of OM in the studied sections, the $\delta^{13}C$ values and Hg concentrations from these sedimentary successions are interpreted to be primary. This is because the $\delta^{13}C$ trends (carbonate and organic carbon) and range in absolute values for the studied successions are consistent with those for other Tethyan Smithian to Spathian sedimentary successions (e.g., Tong et al., 2007; Song et al., 2013). Notably, we find that the global early to middle Smithian negative carbon isotope excursion (CIE) and the positive CIE characteristic of the SSB (N3 and P3, respectively; Song et al., 2013) are recorded in both organic carbon and carbonate carbon isotope records. The reproducibility of the Smithian $\delta^{13}C$ trends in both organic and carbonate carbon supports the argument that the documented geochemical records for these successions are primary.

Similar to the $\delta^{13}C$ record, Hg anomalies that variably span the middle Smithian to SSB are known from both Tethyan and Boreal sedimentary successions (e.g., Grasby et al., 2016; Hammer et al., 2019; Shen et al., 2019a; Wang et al., 2019a). Thus, the spatial reproducibility of Hg enrichment in Smithian rocks globally argues against the possibility that our documented Hg trends can be explained by diagenetic alteration of the studied rocks. Furthermore, there is no correlation between HI and TOC or Hg (Fig. 7), suggesting that the Hg record is not affected to any significant degree by organic matter type or preservation. Therefore, both the CIEs and Hg anomalies recorded in these sections are interpreted as reflecting environmental perturbations that affected the carbon and mercury cycles during the Smithian-Spathian transition.

5.2. *High-resolution correlation of the Tethyan Smithian-Spathian Hg records*

Biostratigraphical correlations based on conodont unitary association zones (UAZ) for sections from Oman and South China recently published by Leu et al. (2022, 2023), together with precise and accurate U—Pb zircon ages for QIA and SHA (Widmann et al., 2020), enable a high-resolution correlation of the geochemical records presented in the current study (Fig. 8). For QIA, the Hg anomaly spans conodont UAZ 6 to UAZ 8, while the positive CIE spans UAZ 7 to UAZ 9. For SHA, the presence of a hiatus at the SSB precludes a determination of the precise onset of the SSB positive CIE (Fig. 8B). Nevertheless, it is apparent that the onset of the positive CIE is younger than UAZ 6 (ca. 249.330 ± 0.100 Ma) and that the CIE climaxes within UAZ 9 (ca. 249.088 ± 0.073 Ma), similar to QIA (Fig. 8). The SHA Hg record indicates that Hg peaks are recorded between UAZ 5 and UAZ 7 (i.e., between 250.116 ± 0.085 Ma and 249.330 ± 0.100 Ma, Widmann et al., 2020), indicating that the onset of Hg enrichment for SHA was earlier than for QIA (Fig. 8). Unlike the South China successions, the Hg enrichment interval recorded for JA is restricted to a brief stratigraphic interval, i.e., UAZ 3 of Oman, which corresponds to the interval of separation between UAZs 7 and 8 of South China (Fig. 8). The SSB positive CIE for JA, however, is stratigraphically extended, spanning UAZs 1 to 5 (which corresponds to UAZs 6 to 9 of South China; Leu et al., 2023). For both QIA and SHA, the onset of the Smithian Hg anomaly predates the onset of the global SSB positive CIE. However, the opposite is true for JA. Therefore, the Hg anomalies

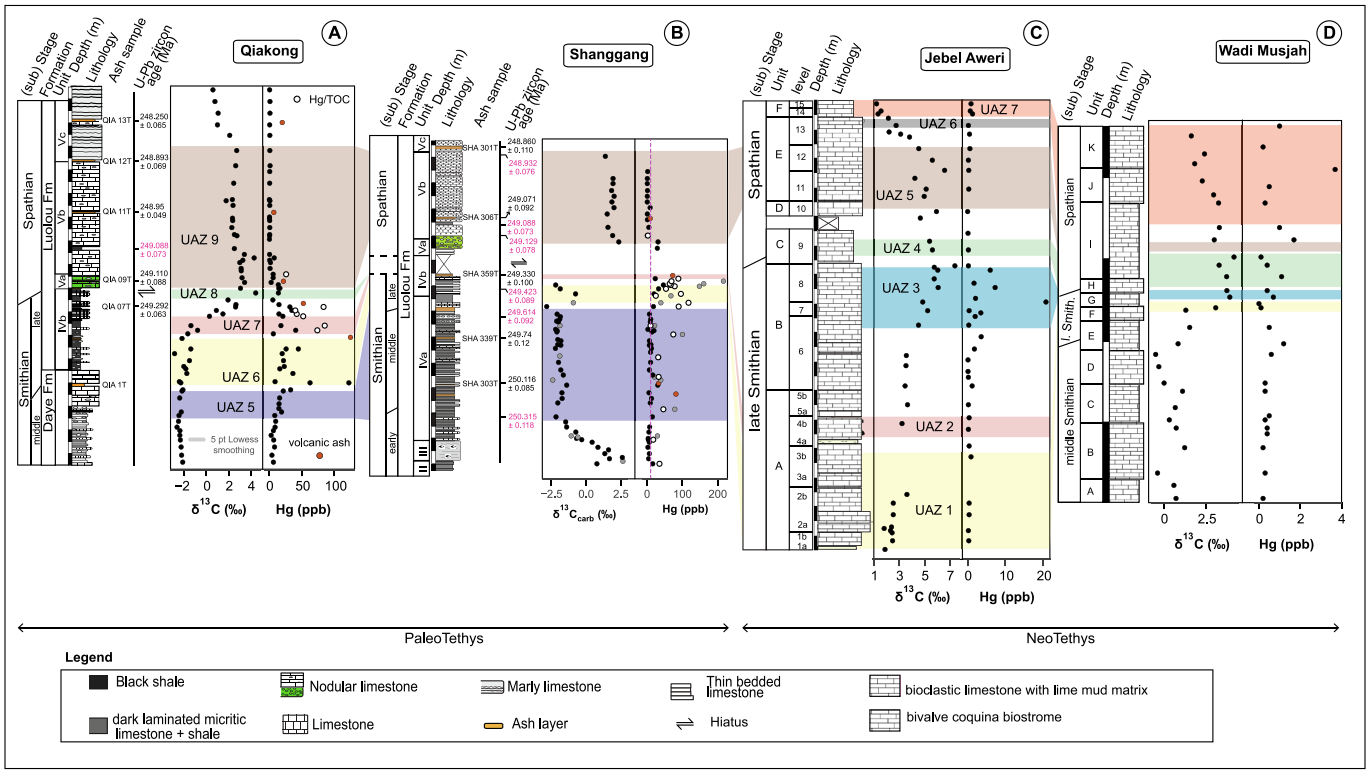

Fig. 8. Carbon isotope ($\delta^{13}C$) and mercury records correlated across the studied sections. $\delta^{13}C$ data, stratigraphic log and U—Pb zircon ages for Qiakong and Shanggang are from Widmann et al. (2020). $\delta^{13}C$ data for Jebel Aweri and Wadi Musjah sections is from Leu et al. (2023). Correlation of the sections follows Leu et al. (2023) and is based on U—Pb zircon ages and conodont unitary association zones.

recorded for these Tethyan sites are temporally discordant, opening the possibility that they may derive from unrelated causes.

Divergence in onset between the SSB positive CIE and Smithian Hg anomalies is documented for other sections in the PaleoTethys (e.g., North Pingdingshan, Zuodeng), the NeoTethys (e.g., Guryul Ravine, Mud) and Panthalassa (e.g., Festningen, Jesmond, Smith Creek) (Fig. 9; see also Grasby et al., 2013b; Grasby et al., 2016; Shen et al., 2019a; Wang et al., 2019a). These observations indicate that the record of Hg anomalies in Smithian to Spathian marine successions is variable in both timing (onset) and duration. In the case of SHA, the offset between the onset of Smithian Hg anomalies and the SSB positive CIE is about 700 kyr (Fig. 8). Thus, the variability in the timing/stratigraphic occurrence of Smithian Hg anomalies contrasts with the carbon isotope record, for which the stratigraphic occurrence of Early Triassic excursions seems to match globally (Zhang et al., 2019). Consequently, Smithian Hg anomalies may be indicative of local patterns of Hg sequestration, which may be unrelated to the causes of the associated CIEs.

5.3. Hosts of Hg and interpretation of the Hg anomaly

5.3.1. Sedimentary hosts of Hg in QIA & SHA

Volcanic eruptions are recognized as the dominant natural source of Hg to the environment (Pyle and Mather, 2003). However, a direct link between volcanic activity and anomalous Hg content in sedimentary strata cannot be assumed. This is because enhanced Hg sequestration in rocks can also occur via non-volcanic means (e.g., Hammer et al., 2019; Them II et al., 2019; Shen et al., 2019b). Also, Hg enrichment in sedimentary successions may result from variations in the abundance of sedimentary host phases of Hg (Shen et al., 2019b, 2020).

Spearman's rank correlation analysis indicates a moderate but significant correlation between Hg and TOC for both SHA and QIA (SHA: $\rho = 0.57$, $p = 0.00$, QIA: $\rho = 0.72$, $p = 0.00$), suggesting a significant influence of organic matter availability on Hg sequestration for both sites (Fig. 4A). In addition, a significant correlation between Hg and Al is noted for SHA, as well as between Hg and U for QIA and SHA (Fig. 4). These correlations suggest that both lithology and OM content modulated Hg sequestration for these successions. Nevertheless, the persistence of the Hg anomaly upon Hg/TOC normalization (where TOC > 0.2 wt% for both QIA and SHA) suggests that Hg enrichment recorded for these successions cannot be explained by OM availability only. Furthermore, although amounts of Hg sequestered appears to be lower in carbonate-rich but OM-poor strata, the recorded Hg anomalies relative to background values are recorded in nodular limestone, shale, and volcanic ash samples alike, just to different degrees (Fig. 2, Fig. S4).

5.3.2. Interpretation of the South China Hg anomaly

Mercury has a complex biogeochemical cycle and can be deposited in the environment via several pathways (Selin, 2009). Different studies indicate that upon initial emission from volcanoes, Hg has no measurable MIF (Zambardi et al., 2009; Sun et al., 2016; Si et al., 2020), in agreement with estimates of the Δ^{199}Hg value of the primitive mantle (Moynier et al., 2021). However, during Hg biogeochemical cycling, diagnostic patterns of isotopic variation are imparted by different processes (such as volatilization, photoreduction and methylation), allowing for the use of Hg isotope ratios to decipher the sources and pathways of Hg deposition (Blum et al., 2014; Yin et al., 2014; but see also Grasby et al., 2019; Percival et al., 2021 and Yager et al., 2021 for a review). Hg in sedimentary rocks that are deposited in marine depositional environments far away from land (or with limited terrigenous input) are usually characterized by positive Δ^{199}Hg values, reflective of a dominantly atmospheric Hg input source (Blum et al., 2014; Sun et al., 2019; Yager et al., 2021). In contrast, marine successions deposited closer to land usually have Hg with negative Δ^{199}Hg values, which is consistent with Hg input from terrestrial biomass (Yager et al., 2021; Yin et al., 2022). Furthermore, a record of near zero Hg MIF in sedimentary successions may indicate that Hg in these rocks was sourced from different reservoirs having complementary MIF values that average to near zero (c.f. Blum et al., 2014).

Near zero Δ^{199}Hg values recorded for QIA and slightly positive values for SHA are consistent with direct volcanic Hg emissions and/or a mixture of Hg contributions from terrestrial biomass and atmospheric Hg inputs to the Nanpanjiang Basin during the studied interval. The late Smithian of the Nanpanjiang Basin is characterized by a 622 ± 137 kyr period of black shale deposition (Widmann et al., 2020), which suggests elevated terrigenous flux to the Nanpanjiang Basin during this interval. Owing to characteristically negative Δ^{199}Hg values for terrestrial biomass, it is reasonable to expect negative Δ^{199}Hg values (or a trend to less positive Δ^{199}Hg values) within the interval of black shale deposition. However, both SHA and QIA are characterized by near zero to slightly positive Δ^{199}Hg values during the Smithian (Fig. 2). In addition, volcanic ashes with no MIF, which show similar Hg concentration trends with interbedded rocks, occur within the late Smithian Hg enrichment interval (Fig. 2). These observations suggest that both QIA and SHA were characterized by atmospheric Hg input, probably from a proximal volcanic Hg source. Similar observations have recently been documented for Permian-Triassic boundary sections in South China (Edward et al., 2023b). Furthermore, an atmospheric volcanic Hg source to the Nanpanjiang Basin during the Smithian is supported by slightly negative Δ^{200}Hg values recorded for some samples from SHA (Fig. 2), which are comparable to those reported for gaseous elemental Hg^0 from atmospheric samples by Rolison et al. (2013). Consequently, the Hg isotope MIF record supports a scenario whereby Hg in these Nanpanjiang Basin sections was sourced from direct atmospheric deposition from volcanic emissions. The trend towards more positive Δ^{199}Hg values for SHA from the middle Smithian to early Spathian, despite elevated late Smithian detrital flux further supports our inference that atmospherically cycled Hg from volcanic activity dominated Hg input to the Nanpanjiang Basin during this interval.

Potential candidates for volcanically sourced Hg to the Nanpanjiang Basin during the Olenekian include renewed STLIP volcanism and subduction-related arc volcanism in the Tethys region. Renewed volcanism of the STLIP has been suggested as an explanation for environmental and climatic perturbation during the Early Triassic (e.g., Payne and Kump, 2007; Paton et al., 2010; Grasby et al., 2013a), as well as for Hg anomalies recorded in Olenekian strata (Grasby et al., 2016; Shen et al., 2019a). However, no tangible proof of purported STLIP volcanism during the Smithian has been found so far (Grasby et al., 2013b; Hammer et al., 2019; Shen et al., 2019a; Widmann et al., 2020). Furthermore, U—Pb zircon age constraint for our Smithian-Spathian Hg records (Fig. 8; Widmann et al., 2020) indicates that the Smithian Hg anomalies recorded in the Nanpanjiang Basin post-date the youngest dated STLIP rocks (ca. 250.3 Ma; Augland et al., 2019). In contrast with renewed STLIP volcanism, direct evidence for near-field volcanic activity in the Tethys region is provided by abundant volcanic ash layers in Smithian to Spathian strata in South China (Galfetti et al., 2007b; Gilder et al., 2008; Ovtcharova et al., 2015; Widmann et al., 2020). These volcanic ashes have similar Hg concentration trends as interbedded Smithian rocks and are also characterized by near zero Hg isotope MIF (Fig. 2). Hence, it is reasonable to suggest that the volcanic effusions that supplied these volcanic ashes was the same as that supplying Hg to the Nanpanjiang Basin during the Smithian – Spathian.

Volcanic ash samples from QIA and SHA are geochemically distinct from STLIP rocks but similar to Permian to Triassic-aged volcanic ashes from other localities in South China (Fig. 5). These ashes plot within the field of rhyodacite/dacite and trachyandesite on a Zr/Ti vs Nb/Y discrimination diagram (Winchester and Floyd, 1977), consistent with the composition of Early Triassic volcanic rocks that outcrop in southern South China (Gilder et al., 2008). The ashes are characterized by notable negative Nb, Ta and Ti anomalies on the primitive mantle-normalized incompatible trace elements plot (Fig. 5A, 5B), consistent with a subduction zone provenance (Pearce et al., 1995). Also, these ash samples plot within the field of arc lavas on the Ti vs Zr diagram (Fig. 5D; Pearce,

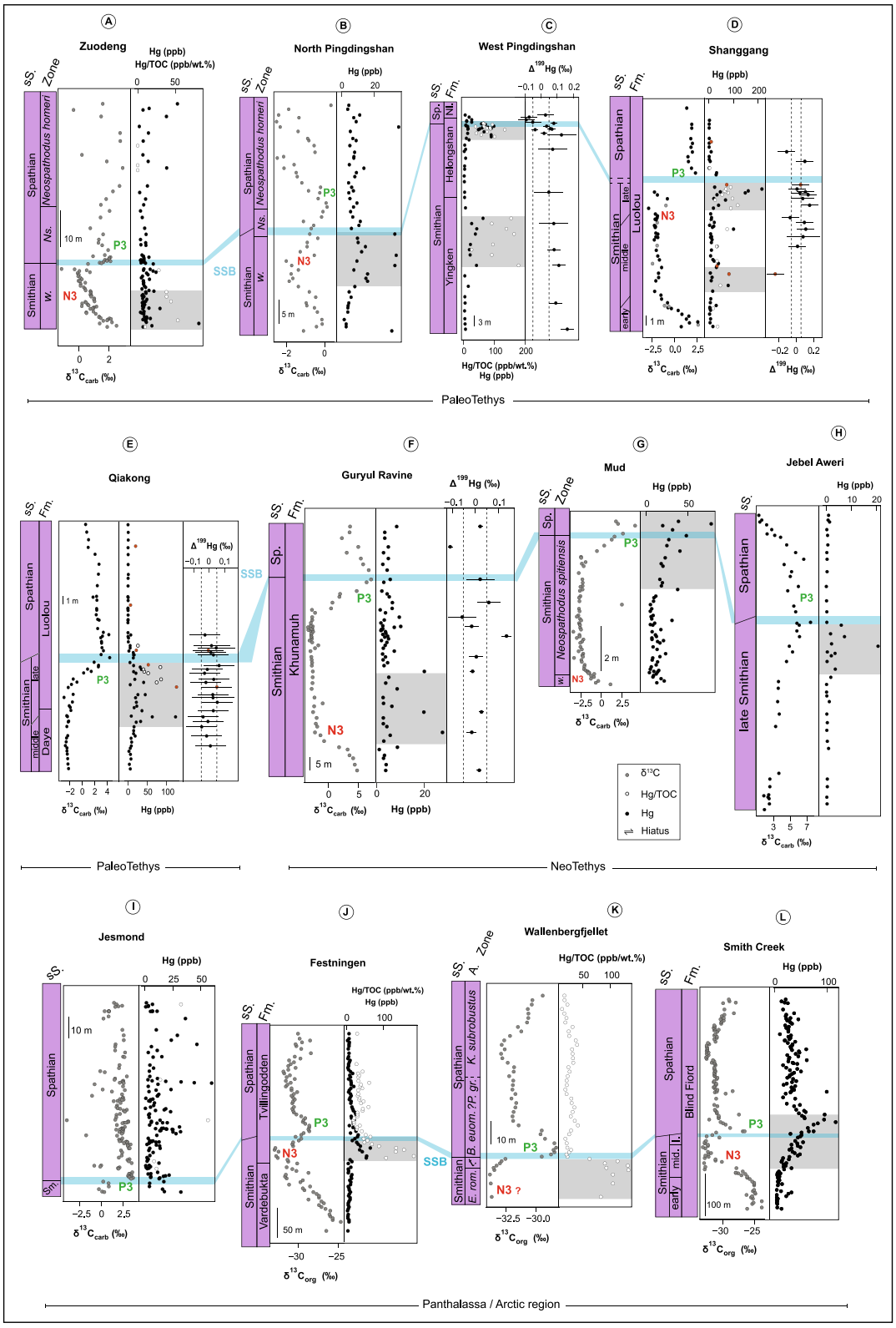

Fig. 9. Compilation of Smithian – Spathian mercury and $\delta^{13}C$ profiles from Tethyan and Boreal sections. A) Zuodeng, B) North Pingdingshan, C) West Pingdingshan, D) Shanggang, E) Qiakong, F) Guryul Ravine, G) Mud, H) Jebel Aweri, I) Jesmond, J) Festningen, K) Wallenbergfjellet, L) Smith Creek. Hg/TOC profiles are only included where reported Hg/TOC values are >0.2 wt%. The sections are correlated using the Smithian-Spathian boundary (SSB) as originally delineated by the authors of the source publications. The horizontal blue band is an uncertainty interval for the placement of the SSB for our correlation. For Festningen, the SSB is delineated by taking the mid-point of the N3 to P3 carbon isotope excursion after Zhang et al. (2019). Data sources are as follows: Guryul Ravine, West Pingdingshan: Wang et al. (2019a); Mud, Zuodeng, North Pingdingshan, Jesmond: Shen et al. (2019a); Wallenbergfjellet: Hammer et al. (2019); Festningen: Grasby et al. (2016); Smith Creek: Grasby et al. (2013a, 2013b). Abbreviations: sS. – sub-Stage, Fm. – Formation, Sp. – Spathian, Sm. – Smithian, mid. – middle, l. – late, Nl. – Nanlinghu, A. – Ammonoid, *w.* – *Novispathodus waageni*, *Ns.* – *Novispathopdus pingdingshanensis*, *t.* – *Wasatchites tardus*, *E. rom.* – *Euflemingites romunderi*, *B. euom.* – *Bajarunia euomphala*, *P. gr.* – *Parasibirites grambergi*. (For interpretation of the references to colour in this figure legend, the reader is referred to the web version of this article.)

1982). As such, QIA and SHA volcanic ashes derive from subduction-related arc volcanism (He et al., 2014), which is documented for the South China region during the Early Triassic (Zi et al., 2013; Duan et al., 2020; Duan et al., 2023). Subduction-related arc volcanism can result in the release of large amounts of volatiles, including Hg, into the atmosphere (Lu et al., 2021; Shen et al., 2021; Zhang et al., 2021), consistent with the frequent occurrence of volcanic ashes in Olenekian strata within South China (Ovtcharova et al., 2006; Widmann et al., 2020). Consequently, it is concluded that subduction-related arc volcanism in the Tethys region was the source of volcanic Hg to the Nanpanjiang Basin during the studied interval.

5.3.3. Interpretation of the Jebel Aweri Hg enrichment interval

Low amounts of OM and absence of a correlation between Hg and Al, as well as redox proxy elements such as Mo and U (Fig. 4), precludes an evaluation of the control of sedimentary Hg hosts on Hg sequestration in the JA succession. The late Smithian Hg enrichment interval for JA is presumably related to factors other than enhanced availability of sedimentary Hg host phases. Furthermore, Hg content in this carbonate succession is generally too low for Hg extraction for isotopic analysis. Despite the generally low Hg content in JA samples, a Hg enrichment interval is inferred because it is expected that this succession be characterized by near zero Hg content owing to its pure carbonate mineralogical composition and depositional environment. The JA succession was deposited on an offshore seamount (Leu et al., 2023), limiting the potential for terrestrial Hg input to this succession (also evidenced by near zero Al and TOC contents, Fig. 4). Also, well-oxygenated depositional environments which are usually impoverished with regards to preserved organic matter and sulfides, and with low clay mineral content, can be expected to have limited Hg sequestration ability (Percival et al., 2018). Hence, considering the depositional setting and mineralogical composition of the JA succession, the Hg enrichment recorded in this succession is significant and unlikely to be sourced from terrestrial runoff. This inference is further compatible with relatively lower $^{87}Sr/^{86}Sr$ values across the interval of Hg enrichment (Fig. 3A), which is opposite of the trend expected during periods of enhanced continental weathering input to the oceans. Although considered only a minor source of Hg to the ocean, hydrothermal vents associated with mid-oceanic ridges may be locally important Hg sources to specific sites (Bowman et al., 2020; Racki, 2020; Sanei et al., 2021). Paleogeographic reconstructions for the Early Triassic after the Panalesis model (Fig. 1B; Vérard, 2019) suggest that the WMJ and JA successions were deposited along a hotspot track close to a mid-oceanic ridge. Also, the trend of higher (more radiogenic) $\varepsilon_{Nd(t)}$ values recorded around the SSB for JA and WMJ (Fig. 3) is consistent with mantle fluxes to these NeoTethyan sites (Bizimis and Scher, 2016). Alternatively, Hg enrichment recorded for JA may be due to nearby submarine volcanic activity (e.g., Scaife et al., 2017; Jones et al., 2019; Racki, 2020). Hence, the latest Smithian Hg enrichment recorded for JA, and positive $\varepsilon_{Nd(t)}$ excursions for WMJ and JA around the SSB (Fig. 3) are compatible with hydrothermal fluid or submarine volcanic Hg input to these offshore seamount carbonate depositional environments. Inferred hydrothermal/submarine volcanic Hg input to JA during the late Smithian is further supported by plume-related magmatic activity associated with late Paleozoic to Triassic rifting of the Gondwana and Cimmerian blocks (Şengör et al., 1984; Stampfli et al., 1991; Chauvet et al., 2008), which was likely associated with hydrothermal fluid circulation in the NeoTethys. The absence of a corresponding Hg enrichment interval for WMJ may indicate that inferred hydrothermal Hg input to NeoTethyan offshore seamount depositional environments during the late Smithian was locally restricted. Alternatively, the existence of a late Smithian Hg enrichment interval for WMJ may be hidden due to the very condensed nature of this carbonate succession.

5.4. Correlation and provenance of global Smithian to Spathian Hg records

The $\delta^{13}C$ record of the middle Smithian to early Spathian interval is well constrained, in that several studies show that this interval is globally marked by a large negative excursion (N3, middle Smithian to early late Smithian), which is succeeded by a large positive excursion (P3) spanning the late Smithian to earliest Spathian (Galfetti et al., 2007b; Tong et al., 2007; Song et al., 2013; Zhang et al., 2019). Hence, the $\delta^{13}C$ trends may be used as a stratigraphic marker to evaluate the timing of other geochemical excursions that may be recorded in coeval strata. In expanded marine sections, the N3 and P3 excursions are usually separated by an interval of nearly uniform $\delta^{13}C$ values (Fig. 9), as can be observed from $\delta^{13}C$ records for Guryul Ravine (Wang et al., 2019a), Mud (Shen et al., 2019a), Yashan (Du et al., 2022), Laren, Qiakong, and Shanggang (Widmann et al., 2020; Dai et al., 2021; Leu et al., 2022). In sharp contrast, the N3 CIE abruptly grades into the late Smithian P3 CIE in some other marine sections such as the North Pingdingshan (Tong et al., 2007), Mingtang (Song et al., 2013), Festningen (Grasby et al., 2016), Wallenbergfjellet (Hammer et al., 2019), Wadi Musjah (Leu et al., 2023), Jesmond (Shen et al., 2019a), and Smith Creek sections (Grasby et al., 2013a), among others. This abrupt transition from N3 to P3 in many sections is strongly suggestive of a late Smithian hiatus (Hammer et al., 2019), a detail that is important when comparing geochemical records between spatially dispersed Smithian to Spathian-aged successions.

Mercury anomalies within Smithian to Spathian strata from both high and low-latitude marine successions have been documented by different workers (e.g., Grasby et al., 2013b; Grasby et al., 2016; Hammer et al., 2019; Shen et al., 2019a; Wang et al., 2019a) and are summarized in Fig. 9. Shen et al. (2019a) documented Smithian Hg anomalies from marine successions straddling the Smithian-Spathian boundary and found that these Hg enrichments coincide with a Smithian negative CIE (N3; Song et al., 2013). These authors argued that the recorded middle Smithian Hg anomalies resulted from STLIP volcanic activity during the Smithian, similar to previous suggestions by Grasby et al. (2013b, 2016) based on Hg records from the Festningen and Smith Creek sections. In contrast, Wang et al. (2019a) recorded a Hg anomaly (not reflected in Hg/TOC ratios) for both the middle Smithian and SSB for one (Chaohu section, South China) of two investigated sections, concluding that any potential renewed STLIP volcanism probably only affected the northern hemisphere. For the Chaohu section, Wang et al. (2019a) document elevated middle Smithian Hg/TOC ratios coincident with a negative CIE (N3) but also late Smithian enrichments coincident with the SSB positive CIE (P3). The global occurrence of Hg anomalies within middle and late Smithian strata, therefore, suggests that the middle to late Smithian interval was characterized by elevated Hg supply to and/or sequestration in Smithian oceans. Nevertheless, a comparison of these Hg records indicates that Smithian Hg anomalies vary in their stratigraphic occurrence between different sections (Fig. 9). Specifically, Smithian Hg anomalies variably correspond stratigraphically to the peak of the N3 CIE or the onset of the P3 CIE (Fig. 9), suggesting that the cause(s) of the global carbon cycle perturbations are not directly related to the stratigraphically variable Hg anomalies. Despite the widespread occurrence of middle to late Smithian Hg anomalies, available evidence indicates that these Hg anomalies differ in provenance. For the South China region, our results, together with those from previous studies (e.g., Shen et al., 2019a; Wang et al., 2019a), suggest that middle to late Smithian Hg anomalies are most likely due to a combination of regional subduction-related volcanism and enhanced terrigenous flux to marine environments presumably due to elevated continental weathering.

Smithian to Spathian increase in continental weathering is supported by the bioapatite $^{87}Sr/^{86}Sr$ record for WMJ, which shows a secular increasing trend from the middle Smithian to Spathian (Fig. 3), consistent with previously published Early Triassic $^{87}Sr/^{86}Sr$ records (e.g.,

Sedlacek et al., 2014; Song et al., 2015). While there is direct evidence for Smithian volcanism in South China, the same cannot be said for other regions. Apart from the Guryul Ravine and West Pingdingshan (Chaohu) sections (Wang et al., 2019a), previously published Smithian–Spathian Hg records lack Hg isotope data, inhibiting more detailed investigation of the provenance of Smithian Hg anomalies documented for these sites. However, for the high-latitude Wallenbergfjellet section, Spitsbergen, Hammer et al. (2019) recently demonstrated that the middle to late Smithian Hg/TOC anomaly recorded for this section is attributable to a change in OM type from terrestrial to marine OM. Furthermore, based on the correlation between Hg and Al, as well as Hg isotope compositions, recorded increases in Smithian Hg/TOC ratios for Chaohu and Guryul Ravine sections were attributed to increased terrestrial Hg flux to Tethyan marine depositional environments during the Early Triassic (Wang et al., 2019a). Variable provenance for Smithian Hg anomalies is further supported by the Smithian Hg enrichment recorded for JA, which can be attributed to submarine volcanic or hydrothermal fluid activity. Therefore, the causes of Hg anomalies recorded during the Smithian vary for different localities. This view is further strengthened by the variability in onset, duration, and magnitude of recorded Smithian Hg anomalies (Fig. 9; Widmann et al., 2020).

6. Conclusions

The temporally calibrated Hg concentration and Hg-, C-, Sr- and Nd-isotope records and other geochemical data for NeoTethyan and PaleoTethyan successions presented in the current study allows for an assessment of the tempo of global Hg sequestration, as well as an evaluation of Hg input sources to the studied successions during the Olenekian. Based on the presented results, the following conclusions are made:

1) The middle Smithian to late Smithian of the Nanpanjiang Basin, South China is characterized by enhanced Hg sequestration recorded by Hg enrichment intervals.
2) The Hg enrichment intervals recorded for these PaleoTethyan sections predate the onset of the SSB positive CIE recorded globally.
3) The Hg enrichment can be attributed mainly to volcanic Hg input from regional subduction-related arc-volcanism and potential contributions from terrestrial Hg reservoirs to the Nanpanjiang Basin.
4) The late Smithian Hg enrichment recorded for the JA succession can be attributed to hydrothermal fluid activity or submarine volcanism proximal to the offshore seamount depositional environment. Thus, the presence of a Hg enrichment interval across both carbonate-poor and carbonate-rich Smithian-aged strata in the PaleoTethys and NeoTethys suggests that although lithology may exert an overarching control on the magnitude of Hg sequestration, marine sedimentary rocks do record primary trends of excess Hg loading to the environment.
5) Smithian Hg anomalies recorded for spatially dispersed localities vary in stratigraphic expression, variably coinciding with either a negative or positive CIE and as such, probably record local Hg sequestration patterns. Consequently, Smithian-Spathian Hg anomalies, although recorded in several localities globally, are of variable provenance and cannot be linked to a singular source such as renewed STLIP volcanism during the Smithian to Spathian.

CRediT authorship contribution statement

Oluwaseun Edward: Conceptualization, Data curation, Formal analysis, Investigation, Visualization, Writing – original draft, Writing – review & editing. **Marc Leu:** Data curation, Validation, Writing – review & editing. **Hugo Bucher:** Funding acquisition, Investigation, Project administration, Resources, Writing – review & editing. **Sandrine Le Houedec:** Investigation, Resources, Validation, Writing – review & editing. **Franziska Blattmann:** Investigation, Validation, Writing – review & editing. **Christian Vérard:** Formal analysis, Resources, Visualization, Writing – review & editing. **Thierry Adatte:** Investigation, Resources, Validation, Writing – review & editing. **Aymon Baud:** Resources, Validation, Writing – review & editing. **Jeroen E. Sonke:** Investigation, Resources, Validation, Writing – review & editing. **Torsten Vennemann:** Conceptualization, Funding acquisition, Project administration, Resources, Supervision, Writing – review & editing.

Declaration of Competing Interest

None.

Data availability

Datasets related to this article can be found at https://dx.doi.org/10.17632/vg9sy4k8jf.2, an open-source online data repository hosted at Mendeley Data (Edward et al., 2023).

Acknowledgements

This study was funded by a Swiss National Science Foundation Sinergia Grant (project nr. CRSII5_180253). SLH gratefully acknowledges financial support by the University of Geneva (S18173). Field assistance by Kuang Guodun and Ji Cheng is gratefully acknowledged. Jun Shen (CUG, Wuhan) is thanked for providing the raw data for his 2019 Earth Science Reviews paper. We also thank Jorge Spangenberg, Jerome Chmeleff, Massimo Chiaradia, and Sophie Michalet for analytical assistance. The authors wish to thank Sofie Lindström and one anonymous reviewer for their constructive comments which improved the manuscript. Efficient editorial handling of this manuscript by the Editor, Maoyan Zhu, is gratefully acknowledged.

Appendix A. Supplementary data

Supplementary data to this article can be found online at https://doi.org/10.1016/j.gloplacha.2023.104343.

References

Adatte, T., Stinnesbeck, W., Keller, G., 1996. Lithostratigraphic and mineralogic correlations of near K/T boundary clastic sediments in northeastern Mexico: implications for origin and nature of deposition. Geol. Soc. Am. Spec. Paper 307, 211–226.

Augland, L.E., Ryabov, V.V., Vernikovsky, V.A., Planke, S., Polozov, A., Callegaro, S., Jerram, D.A., Svensen, H., 2019. The main pulse of the Siberian Traps expanded in size and composition. Sci. Rep. 9, 1–12. https://doi.org/10.1038/s41598-019-54023-2.

Bagherpour, B., Bucher, H., Baud, A., Brosse, M., Vennemann, T., Martini, R., Guodun, K., 2017. Onset, development, and cessation of basal early Triassic microbialites (BETM) in the Nanpanjiang pull-apart Basin, South China Block. Gondw. Res. 44, 178–204. https://doi.org/10.1016/j.gr.2016.11.013.

Bagherpour, B., Bucher, H., Vennemann, T., Schneebeli-Hermann, E., Yuan, D.X., Leu, M., Zhang, C., Shen, S.Z., 2020. Are late Permian carbon isotope excursions of local or of global significance? Geol. Soc. Am. Bull. 132, 521–544. https://doi.org/10.1130/B31996.1.

Baud, A., 2013. The Olenekian (early Triassic) Red Ammonoid Limestone, a time-specific facies on the Gondwana margin: Timor-Roof of the World-Oman connection. Acta Geol. Sin. 87, 894–931. https://doi.org/10.1111/1755-6724.12150_2.

Baud, A., Marcoux, J., Guiraud, R., Ricou, L., Gaetani, M., 1993. Late Murgabian (266 to 264 Ma) Paleoenvironment Map, Explanatory Notes. Gauthier-Villars, Paris.

Baud, A., Béchennec, F., Krystyn, L., Le Métour, J., Marcoux, J., Maury, R., Richoz, S., 2001. Permo-Triassic Deposits: from the Platform to the Basin and Seamounts. Conference on the Geology of Oman, Field guidebook, Excursion A01, Conference on the Geology of Oman, Field guidebook, Excursion A01, pp. 1–54. DOI:https://www.researchgate.net/publication/236624812.

Baud, A., Richoz, S., Beauchamp, B., Cordey, F., Grasby, S., Henderson, C.M., Krystyn, L., Nicora, A., 2012. The Buday'ah Formation, Sultanate of Oman: a Middle Permian to early Triassic oceanic record of the Neotethys and the late Induan microsphere bloom. J. Asian Earth Sci. 43, 130–144. https://doi.org/10.1016/j.jseaes.2011.08.016.

Behar, F., Beaumont, V., Penteado, H.L.D., 2001. Rock-Eval 6 technology: Performances and developments. Oil Gas Sci. Technol. 56, 111–134. https://doi.org/10.2516/ogst:2001013.

Bizimis, M., Scher, H.D., 2016. Neodymium Isotopes. In: White, W.M. (Ed.), Encyclopedia of geochemistry: a comprehensive reference source on the chemistry of the earth. Springer International Publishing, Cham, pp. 1–6.
Blum, J.D., Bergquist, B.A., 2007. Reporting of variations in the natural isotopic composition of mercury. Anal. Bioanal. Chem. 388, 353–359. https://doi.org/10.1007/s00216-007-1236-9.
Blum, J.D., Sherman, L.S., Johnson, M.W., 2014. Mercury isotopes in earth and environmental sciences. Annu. Rev. Earth Planet. Sci. 42 (42), 249–269. https://doi.org/10.1146/annurev-earth-050212-124107.
Bowman, K.L., Lamborg, C.H., Agather, A.M., 2020. A global perspective on mercury cycling in the ocean. Sci. Total Environ. 710, 136166 https://doi.org/10.1016/j.scitotenv.2019.136166.
Brayard, A., Bucher, H., 2015. Permian-Triassic Extinctions and Rediversifications. In: Klug, C., Korn, D., De Baets, K., Kruta, I., Mapes, R.H. (Eds.), Ammonoid Paleobiology: From Macroevolution to Paleogeography. Springer, Netherlands, Dordrecht, pp. 465–473.
Brayard, A., Escarguel, G., Bucher, H., Monnet, C., Brühwiler, T., Goudemand, N., Galfetti, T., Guex, J., 2009. Good genes and good luck: ammonoid diversity and the end-permian mass extinction. Science 325, 1118–1121. https://doi.org/10.1126/science.1174638.
Brosse, M., Bucher, H., Baud, A., Frisk, A.M., Goudemand, N., Hagdorn, H., Nutzel, A., Ware, D., Hautmann, M., 2019. New data from Oman indicate benthic high biomass productivity coupled with low taxonomic diversity in the aftermath of the Permian-Triassic Boundary mass extinction. Lethaia 52, 165–187. https://doi.org/10.1111/let.12281.
Brühwiler, T., Bucher, H., Goudemand, N., Galfetti, T., 2012. Smithian (early Triassic) ammonoid faunas from Exotic Blocks from Oman: taxonomy and biochronology. Palaeontographica. Abteilung A: Palaeozoologie-Stratigraphie 296, 3–107. https://doi.org/10.1127/pala/296/2012/3.
Caro, G., Bourdon, B., Birck, J.-L., Moorbath, S., 2006. High-precision 142Nd/144Nd measurements in terrestrial rocks: constraints on the early differentiation of the Earth's mantle. Geochim. Cosmochim. Acta 70, 164–191. https://doi.org/10.1016/j.gca.2005.08.015.
Charbonnier, G., Morales, C., Duchamp-Alphonse, S., Westermann, S., Adatte, T., Föllmi, K.B., 2017. Mercury enrichment indicates volcanic triggering of Valanginian environmental change. Sci. Rep. 7, 1–6. https://doi.org/10.1038/srep40808.
Charbonnier, G., Adatte, T., Follmi, K.B., Suan, G., 2020. Effect of intense weathering and postdepositional degradation of organic matter on Hg/TOC proxy in organic-rich sediments and its implicationsfor deep-time investigations. Geochemistry Geophysics Geosystems 21. https://doi.org/10.1029/2019GC008707 e2019GC008707.
Chauvet, F., Lapierre, H., Bosch, D., Guillot, S., Mascle, G., Vannay, J.-C., Cotten, J., Brunet, P., Keller, F., 2008. Geochemistry of the Panjal Traps basalts (NW Himalaya): records of the Pangea Permian break-up. Bulletin de la Société géologique de France 179, 383–395. https://doi.org/10.2113/gssgfbull.179.4.383.
Chen, D., Ren, D., Deng, C., Tian, Z., Yin, R., 2022. Mercury loss and isotope fractionation during high-pressure and high-temperature processing of sediments: Implication for the behaviors of mercury during metamorphism. Geochim. Cosmochim. Acta 334, 231–240. https://doi.org/10.1016/j.gca.2022.08.010.
Chen, Z.-Q., Benton, M.J., 2012. The timing and pattern of biotic recovery following the end-Permian mass extinction. Nat. Geosci. 5, 375–383. https://doi.org/10.1038/ngeo1475.
Dai, X., Yuan, Z.W., Brayard, A., Li, M.T., Liu, X.K., Jia, E.H., Du, Y., Song, H.Y., Song, H. J., 2021. Calibrating the late Smithian (early Triassic) crisis: New insights from the Nanpanjiang Basin, South China. Global and Planetary Change 201, 103492. https://doi.org/10.1016/j.gloplacha.2021.103492.
Du, Y., Zhu, Y., Corso, J.D., Huang, J., Qiu, H., Song, H., Tian, L., Chu, D., Tong, J., Song, H., 2022. New early Triassic marine δ13C record from the northeastern Yangtze Platform: implications for contemporaneous temperature changes and volcanic eruptions. Palaeogeogr. Palaeoclimatol. Palaeoecol. 607, 111270 https://doi.org/10.1016/j.palaeo.2022.111270.
Duan, L., Meng, Q.-R., Wu, G.-L., Yang, Z., Wang, J., Zhan, R., 2020. Nanpanjiang basin: a window on the tectonic development of South China during Triassic assembly of the southeastern and eastern Asia. Gondw. Res. 78, 189–209. https://doi.org/10.1016/j.gr.2019.08.009.
Duan, L., Christie-Blick, N., Meng, Q.R., Wu, G.L., Yang, Z., Wang, B., 2023. A back-arc transtensional origin for the Nanpanjiang basin in the pre-Norian Triassic, with implications for the broader intracontinental development of South China. Basin Res. 35, 551–571. https://doi.org/10.1111/bre.12722.
Edward, Oluwaseun, Bucher, Hugo, Leu, Marc, Le Houedec, Sandrine, Blattmann, Franziska, Vérard, Christian, Adatte, Thierry, Baud, Aymon, Sonke, Jeroen, Vennemann, Torsten, 2023a. Dataset for "Evidence for variable provenance of mercury anomalies during the Smithian–Spathian (Olenekian)". Mendeley Data V2. 10.17632/vg9sy4k8jf.2.
Edward, O., Paul, A.N., Bucher, H., Vérard, C., Adatte, T., Sonke, J.E., Schaltegger, U., Vennemann, T., 2023b. Timing and Provenance of Volcanic Fluxes around the Permian-Triassic Boundary Mass Extinction in South China: U-Pb Zircon Geochronology, Volcanic Ash Geochemistry and Mercury Isotopes. Geochem. Geophys. Geosyst. 24 https://doi.org/10.1029/2023GC010912 e2023GC010912.
Enos, P., Lehrmann, D.J., Jiayong, W., Youyi, Y., Jiafei, X., Chaikin, D.H., Minzoni, M., Berry, A.K., Montgomery, P., 2006. Triassic evolution of the Yangtze platform in Guizhou Province, People's Republic of China. In: Enos, P., Lehrmann, D.J., Jiayong, W., Youyi, Y., Jiafei, X., Chaikin, D.H., Minzoni, M., Berry, A.K., Montgomery, P. (Eds.), Triassic Evolution of the Yangtze Platform in Guizhou Province, People's Republic of China. Geological Society of America.
Erwin, D.H., Bowring, S.A., Yugan, J., 2002. End-Permian mass extinctions: A review. In: Koeberl, C., MacLeod, K.G. (Eds.), Catastrophic Events and Mass Extinctions: Impacts and Beyond. Geological Society of America.
Espitalié, J., Deroo, G., Marquis, F., 1985. La pyrolyse Rock-Eval et ses applications. Rev. Inst. Fr. Pétr 40, 563–579. https://doi.org/10.2516/ogst:1985035.
Fantasia, A., Föllmi, K.B., Adatte, T., Bernárdez, E., Spangenberg, J.E., Mattioli, E., 2018. The Toarcian Oceanic Anoxic Event in southwestern Gondwana: an example from the Andean Basin, northern Chile. J. Geol. Soc. London 175, 883–902. https://doi.org/10.1144/jgs2018-008.
Foster, W.J., Sebe, K., 2017. Recovery and diversification of marine communities following the late Permian mass extinction event in the western Palaeotethys. Global Planet. Change 155, 165–177. https://doi.org/10.1016/j.gloplacha.2017.07.009.
Friesenbichler, E., Hautmann, M., Bucher, H., 2021. The main stage of recovery after the end-Permian mass extinction: Taxonomic rediversification and ecologic reorganization of marine level-bottom communities during the Middle Triassic. PeerJ 9, e11654. https://doi.org/10.7717/peerj.11654.
Galfetti, T., Bucher, H., Brayard, A., Hochuli, P.A., Weissert, H., Guodun, K., Atudorei, V., Guex, J., 2007a. Late early Triassic climate change: insights from carbonate carbon isotopes, sedimentary evolution and ammonoid paleobiogeography. Palaeogeography, Palaeoclimatology, Palaeoecology 243, 394–411. https://doi.org/10.1016/j.palaeo.2006.08.014.
Galfetti, T., Bucher, H., Ovtcharova, M., Schaltegger, U., Brayard, A., Brühwiler, T., Goudemand, N., Weissert, H., Hochuli, P.A., Cordey, F., 2007b. Timing of the Early Triassic carbon cycle perturbations inferred from new U–Pb ages and ammonoid biochronozones. Earth Planet. Sci. Lett. 258, 593–604.
Galfetti, T., Bucher, H., Martini, R., Hochuli, P.A., Weissert, H., Crasquin-Soleau, S., Brayard, A., Goudemand, N., Bruehwiler, T., Guodun, K., 2008. Evolution of early Triassic outer platform paleoenvironments in the Nanpanjiang Basin (South China) and their significance for the biotic recovery. Sediment. Geol. 204, 36–60. https://doi.org/10.1016/j.sedgeo.2007.12.008.
Gilder, S.A., Tan, X., Bucher, H., Kuang, G., Yin, J., 2008. Optimization of apparent polar wander paths: an example from the South China plate. Phys. Earth Planet. In. 169, 166–177. https://doi.org/10.1016/j.pepi.2008.07.016.
Goudemand, N., Romano, C., Leu, M., Bucher, H., Trotter, J.A., Williams, I.S., 2019. Dynamic interplay between climate and marine biodiversity upheavals during the early Triassic Smithian -Spathian biotic crisis. Earth-Science Reviews 195, 169–178. https://doi.org/10.1016/j.earscirev.2019.01.013.
Grasby, S.E., Beauchamp, B., Embry, A., Sanei, H., 2013a. Recurrent early triassic ocean anoxia. Geology 41, 175–178. https://doi.org/10.1130/G33599.1.
Grasby, S.E., Sanei, H., Beauchamp, B., Chen, Z., 2013b. Mercury deposition through the Permo–Triassic biotic crisis. Chem. Geol. 351, 209–216. https://doi.org/10.1016/j.chemgeo.2013.05.022.
Grasby, S.E., Beauchamp, B., Bond, D.P., Wignall, P.B., Sanei, H., 2016. Mercury anomalies associated with three extinction events (Capitanian crisis, latest Permian extinction and the Smithian/Spathian extinction) in NW Pangea. Geol. Mag. 153, 285–297. https://doi.org/10.1017/S0016756815000436.
Grasby, S.E., Them II, T.R., Chen, Z., Yin, R., Ardakani, O.H., 2019. Mercury as a proxy for volcanic emissions in the geologic record. Earth Sci. Rev. https://doi.org/10.1016/j.earscirev.2019.102880, 102880.
Hammer, Ø., Jones, M.T., Schneebeli-Hermann, E., Hansen, B.B., Bucher, H., 2019. Are early Triassic extinction events associated with mercury anomalies? A reassessment of the Smithian/Spathian boundary extinction. Earth-Science Reviews 195, 179–190. https://doi.org/10.1016/j.earscirev.2019.04.016.
Hauser, M., Martini, R., Matter, A., Krystyn, L., Peters, T., Stampfli, G., Zaninetti, L., 2002. The break-up of East Gondwana along the northeast coast of Oman: evidence from the Batain basin. Geol. Mag. 139, 145–157. https://doi.org/10.1017/S0016756801006264.
Hautmann, M., Bagherpour, B., Brosse, M., Frisk, Å., Hofmann, R., Baud, A., Nützel, A., Goudemand, N., Bucher, H., 2015. Competition in slow motion: the unusual case of benthic marine communities in the wake of the end-P ermian mass extinction. Palaeontology 58, 871–901. https://doi.org/10.1111/pala.12186.
He, B., Zhong, Y.T., Xu, Y.G., Li, X.H., 2014. Triggers of Permo-Triassic boundary mass extinction in South China: the Siberian Traps or Paleo-Tethys ignimbrite flare-up? Lithos 204, 258–267. https://doi.org/10.1016/j.lithos.2014.05.011.
Hermann, E., Hochuli Peter, A., Bucher, H., Brühwiler, T., Hautmann, M., Ware, D., Weissert, H., Roohi, G., Yaseen, A., Khalil-ur-Rehman, N., 2012. Climatic oscillations at the onset of the Mesozoic inferred from palynological records from the North Indian Margin. Journal of the Geological Society 169, 227–237. https://doi.org/10.1144/0016-76492010-130.
Hochuli, P.A., Sanson-Barrera, A., Schneebeli-Hermann, E., Bucher, H., 2016. Severest crisis overlooked—Worst disruption of terrestrial environments postdates the Permian–Triassic mass extinction. Sci. Rep. 6, 28372. https://doi.org/10.1038/srep28372.
Hong, H., Algeo, T.J., Fang, Q., Zhao, L., Ji, K., Yin, K., Wang, C., Cheng, S., 2019. Facies dependence of the mineralogy and geochemistry of altered volcanic ash beds: an example from Permian-Triassic transition strata in southwestern China. Earth-Science Reviews 190, 58–88. https://doi.org/10.1016/j.earscirev.2018.12.007.
Immenhauser, A., Schreurs, G., Peters, T., Matter, A., Hauser, M., Dumitrică, P., 1998. Stratigraphy, sedimentology and depositional environments of the Permian to uppermost cretaceous Batain Group. Eclogae Geol. Helv. 91, 217–236. https://doi.org/10.7892/boris.87096.
Jiskra, M., Sonke, J.E., Agnan, Y., Helmig, D., Obrist, D., 2019. Insights from mercury stable isotopes on terrestrial-atmosphere exchange of Hg(0) in the Arctic tundra. Biogeosciences 16, 4051–4064. https://doi.org/10.5194/bg-16-4051-2019.
Jiskra, M., Heimburger-Boavida, L.E., Desgranges, M.M., Petrova, M.V., Dufour, A., Ferreira-Araujo, B., Masbou, J., Chmeleff, J., Thyssen, M., Point, D., Sonke, J.E.,

2021. Mercury stable isotopes constrain atmospheric sources to the ocean. Nature 597, 678–682. https://doi.org/10.1038/s41586-021-03859-8.
Jones, M.T., Percival, L.M.E., Stokke, E.W., Frieling, J., Mather, T.A., Riber, L., Schubert, B.A., Schultz, B., Tegner, C., Planke, S., Svensen, H.H., 2019. Mercury anomalies across the Palaeocene–Eocene Thermal Maximum. Clim. Past 15, 217–236. https://doi.org/10.5194/cp-15-217-2019.
Kübler, B., 1983. Dosage quantitatif des minéraux majeurs des roches sédimentaires par diffraction X. Cahiers de l'Institut de Géologie Series AX 1–13.
Lapierre, H., Samper, A., Bosch, D., Maury, R.C., Béchennec, F., Cotten, J., Demant, A., Brunet, P., Keller, F., Marcoux, J., 2004. The Tethyan plume: geochemical diversity of Middle Permian basalts from the Oman rifted margin. Lithos 74, 167–198. https://doi.org/10.1016/j.lithos.2004.02.006.
Lehrmann, D.J., Jiayong, W., Enos, P., 1998. Controls on facies architecture of a large Triassic carbonate platform; the Great Bank of Guizhou, Nanpanjiang Basin, South China. J. Sediment. Res. 68, 311–326. https://doi.org/10.2110/jsr.68.311.
Lehrmann, D.J., Donghong, P., Enos, P., Minzoni, M., Ellwood, B.B., Orchard, M.J., Jiyan, Z., Jiayong, W., Dillett, P., Koenig, J., 2007. Impact of differential tectonic subsidence on isolated carbonate-platform evolution: Triassic of the Nanpanjiang Basin, South China. AAPG Bull. 91, 287–320. https://doi.org/10.1306/10160606065.
Leu, M., Bucher, H., Goudemand, N., 2019. Clade-dependent size response of conodonts to environmental changes during the late Smithian extinction. Earth-Science Reviews 195, 52–67. https://doi.org/10.1016/j.earscirev.2018.11.003.
Leu, M., Bucher, H., Vennemann, T., Bagherpour, B., Ji, C., Brosse, M., Goudemand, N., 2022. A Unitary Association-based conodont biozonation of the Smithian–Spathian boundary (Early Triassic) and associated biotic crisis from South China. Swiss Journal of Palaeontology 141, 19. https://doi.org/10.1186/s13358-022-00259-x.
Leu, M., Bucher, H., Baud, A., Vennemann, T., Luz, Z., Hautmann, M., Goudemand, N., 2023. An expanded Smithian–Spathian (Lower Triassic) boundary from a reefal build-up record in Oman: implications for conodont taxonomy, high-resolution biochronology and the carbon isotope record. Papers in Palaeontology 9, e1481. https://doi.org/10.1002/spp2.1481.
Lindström, S., Bjerager, M., Alsen, P., Sanei, H., Bojesen-Koefoed, J., 2020. The Smithian–Spathian boundary in North Greenland: implications for extreme global climate changes. Geol. Mag. 157, 1547–1567. https://doi.org/10.1017/S0016756819000669.
Lu, J., Zhou, K., Yang, M., Zhang, P., Shao, L., Hilton, J., 2021. Records of organic carbon isotopic composition (δ13Corg) and volcanism linked to changes in atmospheric pCO2 and climate during the late Paleozoic Icehouse. Global Planet. Change 207, 103654. https://doi.org/10.1016/j.gloplacha.2021.103654.
Martin, E.E., Macdougall, J.D., 1995. Sr and Nd isotopes at the prmian/triassic boundary: a record of climate change. Chem. Geol. 125, 73–99. https://doi.org/10.1016/0009-2541(95)00081-V.
McArthur, J.M., Howarth, R.J., Bailey, T.R., 2001. Strontium isotope stratigraphy: LOWESS version 3: best fit to the marine Sr-isotope curve for 0-509 Ma and accompanying look-up table for deriving numerical age. J. Geol. 109, 155–170. https://doi.org/10.1086/319243.
Moynier, F., Jackson, M.G., Zhang, K., Cai, H., Halldórsson, S.A., Pik, R., Day, J.M.D., Chen, J., 2021. The Mercury Isotopic Composition of Earth's Mantle and the use of Mass Independently Fractionated Hg to Test for Recycled Crust. Geophys. Res. Lett. 48 https://doi.org/10.1029/2021GL094301 e2021GL094301.
Orchard, M.J., 2007. Conodont diversity and evolution through the latest Permian and early Triassic upheavals. Palaeogeography, Palaeoclimatology, Palaeoecology 252, 93–117. https://doi.org/10.1016/j.palaeo.2006.11.037.
Ovtcharova, M., Bucher, H., Schaltegger, U., Galfetti, T., Brayard, A., Guex, J., 2006. New early to Middle Triassic U-Pb ages from South China: calibration with ammonoid biochronozones and implications for the timing of the Triassic biotic recovery. Earth Planet. Sci. Lett. 243, 463–475. https://doi.org/10.1016/j.epsl.2006.01.042.
Ovtcharova, M., Goudemand, N., Hammer, Ø., Guodun, K., Cordey, F., Galfetti, T., Schaltegger, U., Bucher, H., 2015. Developing a strategy for accurate definition of a geological boundary through radio-isotopic and biochronological dating: The Early–Middle Triassic boundary (South China). Earth-Science Reviews 146, 65–76. https://doi.org/10.1016/j.earscirev.2015.03.006.
Paton, M.T., Ivanov, A.V., Fiorentini, M.L., McNaughton, N.J., Mudrovska, I., Reznitskii, L.Z., Demonterova, E.I., 2010. Late Permian and Early Triassic magmatic pulses in the Angara–Taseeva syncline, Southern Siberian Traps and their possible influence on the environment. Russ. Geol. Geophys. 51, 1012–1020. https://doi.org/10.1016/j.rgg.2010.08.009.
Payne, J.L., Kump, L.R., 2007. Evidence for recurrent early Triassic massive volcanism from quantitative interpretation of carbon isotope fluctuations. Earth Planet. Sci. Lett. 256, 264–277. https://doi.org/10.1016/j.epsl.2007.01.034.
Payne, J.L., Lehrmann, D.J., Wei, J., Orchard, M.J., Schrag, D.P., Knoll, A.H., 2004. Large Perturbations of the Carbon Cycle during Recovery from the End-Permian Extinction. Science 305, 506–509. https://doi.org/10.1126/science.1097023.
Pearce, J.A., 1982. Trace element characteristics of lavas from destructive plate boundaries. In: Thorpe, R.S. (Ed.), Orogenic Andesites and Related Rocks. John Wiley and Sons, Chichester, England, pp. 528–548.
Pearce, J.A., Baker, P.E., Harvey, P.K., Luff, I.W., 1995. Geochemical evidence for subduction fluxes, mantle melting and fractional crystallization beneath the South Sandwich island arc. J. Petrol. 36, 1073–1109. https://doi.org/10.1093/petrology/36.4.1073.
Percival, L.M., Jenkyns, H.C., Mather, T.A., Dickson, A.J., Batenburg, S.J., Ruhl, M., Hesselbo, S.P., Barclay, R., Jarvis, I., Robinson, S.A., 2018. Does large igneous province volcanism always perturb the mercury cycle? Comparing the records of Oceanic Anoxic event 2 and the end-cretaceous to other Mesozoic events. Am. J. Sci. 318, 799–860. https://doi.org/10.2475/08.2018.01.
Percival, L.M.E., Bergquist, B.A., Mather, T.A., Sanei, H., 2021. Sedimentary Mercury Enrichments as a Tracer of large Igneous Province Volcanism. In: Ernst, Richard E., Dickson, Alexander J., Bekker, A. (Eds.), Large Igneous Provinces. John Wiley and Sons, Inc., pp. 247–262
Pillevuit, A., Marcoux, J., Stampfli, G., Baud, A., 1997. The Oman Exotics: a key to the understanding of the Neotethyan geodynamic evolution. Geodin. Acta 10, 209–238. https://doi.org/10.1080/09853111.1997.11105303.
Pin, C., Bassin, C., 1992. Evaluation of a strontium-specific extraction chromatographic method for isotopic analysis in geological materials. Anal. Chim. Acta 269, 249–255. https://doi.org/10.1016/0003-2670(92)85409-Y.
Portnyagin, M.V., Ponomareva, V.V., Zelenin, E.A., Bazanova, L.I., Pevzner, M.M., Plechova, A.A., Rogozin, A.N., Garbe-Schönberg, D., 2020. TephraKam: geochemical database of glass compositions in tephra and welded tuffs from the Kamchatka volcanic arc (northwestern Pacific). Earth System Science Data 12, 469–486. https://doi.org/10.5194/essd-12-469-2020.
Pyle, D.M., Mather, T.A., 2003. The importance of volcanic emissions for the global atmospheric mercury cycle. Atmos. Environ. 37, 5115–5124. https://doi.org/10.1016/j.atmosenv.2003.07.011.
Racki, G., 2020. A volcanic scenario for the Frasnian–Famennian major biotic crisis and other Late Devonian global changes: More answers than questions? Global Planet. Change 189, 103174. https://doi.org/10.1016/j.gloplacha.2020.103174.
Richoz, S., Krystyn, L., Baud, A., Brandner, R., Horacek, M., Mohtat-Aghai, P., 2010. Permian–Triassic boundary interval in the Middle East (Iran and N. Oman): progressive environmental change from detailed carbonate carbon isotope marine curve and sedimentary evolution. J. Asian Earth Sci. 39, 236–253. https://doi.org/10.1016/j.jseaes.2009.12.014.
Richoz, S., Baud, A., Beauchamp, B., Grasby, S., Henderson, C., Krystyn, L., 2014. Khuff Margin: Slope to Oceanic Deposits (Permian-Triassic Allochthons and Exotics, Oman). The Khuff Formation: New Perspective: Houten, Netherlands, vol. 1. EAGE Publications, pp. 55–76.
Rolison, J., Landing, W., Luke, W., Cohen, M., Salters, V., 2013. Isotopic composition of species-specific atmospheric Hg in a coastal environment. Chem. Geol. 336, 37–49. https://doi.org/10.1016/j.chemgeo.2012.10.007.
Romano, C., Goudemand, N., Vennemann, T.W., Ware, D., Schneebeli-Hermann, E., Hochuli, P.A., Brühwiler, T., Brinkmann, W., Bucher, H., 2013. Climatic and biotic upheavals following the end-Permian mass extinction. Nat. Geosci. 6, 57–60. https://doi.org/10.1038/ngeo1667.
Sanei, H., Outridge, P.M., Oguri, K., Stern, G.A., Thamdrup, B., Wenzhöfer, F., Wang, F., Glud, R.N., 2021. High mercury accumulation in deep-ocean hadal sediments. Sci. Rep. 11, 10970. https://doi.org/10.1038/s41598-021-90459-1.
Scaife, J.D., Ruhl, M., Dickson, A.J., Mather, T.A., Jenkyns, H.C., Percival, L.M.E., Hesselbo, S.P., Cartwright, J., Eldrett, J.S., Bergman, S.C., Minisini, D., 2017. Sedimentary Mercury Enrichments as a Marker for Submarine large Igneous Province Volcanism? Evidence from the Mid-Cenomanian Event and Oceanic Anoxic Event 2 (late cretaceous). Geochem. Geophys. Geosyst. 18, 4253–4275. https://doi.org/10.1002/2017GC007153.
Scharf, A., Mattern, F., Al-Wardi, M., Frijia, G., Moraetis, D., Pracejus, B., Bauer, W., Callegari, I., 2021. The Geology and Tectonics of the Jabal Akhdar and Saih Hatat Domes, Oman Mountains. Geological Society of London. https://doi.org/10.1144/M54.
Schreurs, G., Immenhauser, A., 1999. West-northwest directed obduction of the Batain Group on the eastern Oman continental margin at the Cretaceous-Tertiary boundary. Tectonics 18, 148–160. https://doi.org/10.1029/1998TC900020.
Sedlacek, A.R., Saltzman, M.R., Algeo, T.J., Horacek, M., Brandner, R., Foland, K., Denniston, R.F., 2014. 87Sr/86Sr stratigraphy from the early Triassic of Zal, Iran: linking temperature to weathering rates and the tempo of ecosystem recovery. Geology 42, 779–782.
Selin, N.E., 2009. Global biogeochemical cycling of Mercury: a review. Annu. Rev. Env. Resour. 34, 43–63. https://doi.org/10.1146/annurev.environ.051308.084314.
Şengör, A.M.C., Yılmaz, Y., Sungurlu, O., 1984. Tectonics of the Mediterranean Cimmerides: nature and evolution of the western termination of Palaeo-Tethys. Geol. Soc. Lond. Spec. Publ. 17, 77–112. https://doi.org/10.1144/GSL.SP.1984.017.01.04.
Shen, J., Algeo, T.J., Planaysky, N.J., Yu, J.X., Feng, Q.L., Song, H.J., Song, H.Y., Rowe, H., Zhou, L., Chen, J.B., 2019a. Mercury enrichments provide evidence of early Triassic volcanism following the end-Permian mass extinction. Earth-Science Reviews 195, 191–212. https://doi.org/10.1016/j.earscirev.2019.05.010.
Shen, J., Algeo, T.J., Chen, J., Planavsky, N.J., Feng, Q., Yu, J., Liu, J., 2019b. Mercury in marine Ordovician/Silurian boundary sections of South China is sulfide-hosted and non-volcanic in origin. Earth Planet. Sci. Lett. 511, 130–140. https://doi.org/10.1016/j.epsl.2019.01.028.
Shen, J., Feng, Q.L., Algeo, T.J., Liu, J.L., Zhou, C.Y., Wei, W., Liu, J.S., Them, T.R., Gill, B.C., Chen, J.B., 2020. Sedimentary host phases of mercury (Hg) and implications for use of Hg as a volcanic proxy. Earth Planet. Sci. Lett. 543, 116333 https://doi.org/10.1016/j.epsl.2020.116333.
Shen, J., Chen, J., Algeo, T.J., Feng, Q., Yu, J., Xu, Y.-G., Xu, G., Lei, Y., Planavsky, N.J., Xie, S., 2021. Mercury fluxes record regional volcanism in the South China craton prior to the end-Permian mass extinction. Geology 49, 452–456. https://doi.org/10.1130/G48501.1.
Si, M., McLagan, D.S., Mazot, A., Szponar, N., Bergquist, B., Lei, Y.D., Mitchell, C.P.J., Wania, F., 2020. Measurement of Atmospheric Mercury over Volcanic and Fumarolic Regions on the North Island of New Zealand using Passive Air Samplers. Acs Earth Space Chem 4, 2435–2443. https://doi.org/10.1021/acsearthspacechem.0c00274.

Smith, A.G., Smith, D.G., Funnell, B.M., 2004. Atlas of Mesozoic and Cenozoic Coastlines. Cambridge University Press.
Song, H., Tong, J., Algeo, T.J., Horacek, M., Qiu, H., Song, H., Tian, L., Chen, Z.-Q., 2013. Large vertical δ13CDIC gradients in early Triassic seas of the South China craton: Implications for oceanographic changes related to Siberian Traps volcanism. Global Planet. Change 105, 7–20. https://doi.org/10.1016/j.gloplacha.2012.10.023.
Song, H., Wignall, P.B., Tong, J., Song, H., Chen, J., Chu, D., Tian, L., Luo, M., Zong, K., Chen, Y., Lai, X., Zhang, K., Wang, H., 2015. Integrated Sr isotope variations and global environmental changes through the late Permian to early late Triassic. Earth Planet. Sci. Lett. 424, 140–147. https://doi.org/10.1016/j.epsl.2015.05.035.
Song, Q., Hong, H., Algeo, T.J., Fang, Q., Zhao, C., Liu, C., Xu, Y., 2022. Clay mineralogy mediated by pH and chemical weathering intensity of Permian–Triassic boundary K-bentonites at Dongpan (Guangxi, South China). Chem. Geol. https://doi.org/10.1016/j.chemgeo.2022.121262, 121262.
Sonke, J.E., Schafer, J., Chmeleff, J., Audry, S., Blanc, G., Dupre, B., 2010. Sedimentary mercury stable isotope records of atmospheric and riverine pollution from two major European heavy metal refineries. Chem. Geol. 279, 90–100. https://doi.org/10.1016/j.chemgeo.2010.09.017.
Spangenberg, J.E., Herlec, U., 2006. Hydrocarbon biomarkers in the Topla-Mezica zinc-lead deposits, northern Karavanke/Drau range, Slovenia: paleoenvironment at the site of ore formation. Econ. Geol. 101, 997–1021. https://doi.org/10.2113/gsecongeo.101.5.997.
Stampfli, G., Marcoux, J., Baud, A., 1991. Tethyan margins in space and time. Palaeogeography, Palaeoclimatology, Palaeoecology 87, 373–409. https://doi.org/10.1016/0031-0182(91)90142-E.
Stampfli, G.M., 2000. Tethyan oceans. Geol. Soc. Lond. Spec. Publ. 173, 1–23. https://doi.org/10.1144/GSL.SP.2000.173.01.01.
Stampfli, G.M., Hochard, C., Vérard, C., Wilhem, C., vonRaumer, J., 2013. The formation of Pangea. Tectonophysics 593, 1–19. https://doi.org/10.1016/j.tecto.2013.02.037.
Stanley, S.M., 2009. Evidence from ammonoids and conodonts for multiple early Triassic mass extinctions. Proc. Natl. Acad. Sci. 106, 15264–15267. https://doi.org/10.1073/pnas.0907992106.
Stanley, S.M., 2016. Estimates of the magnitudes of major marine mass extinctions in earth history. Proc. Natl. Acad. Sci. 113, E6325–E6334. https://doi.org/10.1073/pnas.1613094113.
Sun, R., Enrico, M., Heimburger, L.E., Scott, C., Sonke, J.E., 2013. A double-stage tube furnace–acid-trapping protocol for the pre-concentration of mercury from solid samples for isotopic analysis. Anal. Bioanal. Chem. 405, 6771–6781. https://doi.org/10.1007/s00216-013-7152-2.
Sun, R., Sonke, J.E., Heimbürger, L.-E., Belkin, H.E., Liu, G., Shome, D., Cukrowska, E., Liousse, C., Pokrovsky, O.S., Streets, D.G., 2014. Mercury stable isotope signatures of world coal deposits and historical coal combustion emissions. Environ. Sci. Technol. 48, 7660–7668. https://doi.org/10.1021/es501208a.
Sun, R., Streets, D.G., Horowitz, H.M., Amos, H.M., Liu, G., Perrot, V., Toutain, J.-P., Hintelmann, H., Sunderland, E.M., Sonke, J.E., 2016. Historical (1850–2010) mercury stable isotope inventory from anthropogenic sources to the atmosphereMercury isotope emission inventory. Elementa: Science of the Anthropocene 4. https://doi.org/10.12952/journal.elementa.000091.
Sun, R.Y., Jiskra, M., Amos, H.M., Zhang, Y.X., Sunderland, E.M., Sonke, J.E., 2019. Modelling the mercury stable isotope distribution of Earth surface reservoirs: Implications for global Hg cycling. Geochim. Cosmochim. Acta 246, 156–173. https://doi.org/10.1016/j.gca.2018.11.036.
Sun, S.-S., McDonough, W.F., 1989. Chemical and isotopic systematics of oceanic basalts: implications for mantle composition and processes. Geol. Soc. Lond. Spec. Publ. 42, 313–345. https://doi.org/10.1144/GSL.SP.1989.042.01.1.
Sun, Y., Joachimski, M.M., Wignall, P.B., Yan, C., Chen, Y., Jiang, H., Wang, L., Lai, X., 2012. Lethally Hot Temperatures during the early Triassic Greenhouse. Science 338, 366–370. https://doi.org/10.1126/science.1224126.
Tanaka, T., Togashi, S., Kamioka, H., Amakawa, H., Kagami, H., Hamamoto, T., Yuhara, M., Orihashi, Y., Yoneda, S., Shimizu, H., Kunimaru, T., Takahashi, K., Yanagi, T., Nakano, T., Fujimaki, H., Shinjo, R., Asahara, Y., Tanimizu, M., Dragusanu, C., 2000. JNdi-1: a neodymium isotopic reference in consistency with LaJolla neodymium. Chem. Geol. 168, 279–281. https://doi.org/10.1016/S0009-2541(00)00198-4.
Them II, T., Jagoe, C., Caruthers, A., Gill, B., Grasby, S., Gröcke, D., Yin, R., Owens, J., 2019. Terrestrial sources as the primary delivery mechanism of mercury to the oceans across the Toarcian Oceanic Anoxic Event (early Jurassic). Earth Planet. Sci. Lett. 507, 62–72. https://doi.org/10.1016/j.epsl.2018.11.029.
Tong, J.N., Zuo, J.X., Chen, Z.Q., 2007. Early Triassic carbon isotope excursions from South China: proxies for devastation and restoration of marine ecosystems following the end-Permian mass extinction. Geological Journal 42, 371–389. https://doi.org/10.1002/gj.1084.
Vérard, C., 2019. Panalesis: towards global synthetic palaeogeographies using integration and coupling of manifold models. Geol. Mag. 156, 320–330. https://doi.org/10.1017/S0016756817001042.
Vickers, M.L., Jelby, M.E., Śliwińska, K.K., Percival, L.M., Wang, F., Sanei, H., Price, G. D., Ullmann, C.V., Grasby, S.E., Reinhardt, L., 2023. Volcanism and carbon cycle perturbations in the High Arctic during the Late Jurassic–Early Cretaceous. Palaeogeography, Palaeoclimatology, Palaeoecology 613, 111412. https://doi.org/10.1016/j.palaeo.2023.111412.
Wang, X., Cawood, P.A., Zhao, H., Zhao, L., Grasby, S.E., Chen, Z.-Q., Zhang, L., 2019a. Global mercury cycle during the end-Permian mass extinction and subsequent early Triassic recovery. Earth Planet. Sci. Lett. 513, 144–155. https://doi.org/10.1016/j.epsl.2019.02.026.
Wang, X., Cawood, P.A., Zhao, L., Chen, Z.-Q., Lyu, Z., Ma, B., 2019b. Convergent continental margin volcanic source for ash beds at the Permian-Triassic boundary, South China: Constraints from trace elements and Hf-isotopes. Palaeogeography, Palaeoclimatology, Palaeoecology 519, 154–165. https://doi.org/10.1016/j.palaeo.2018.02.011.
Wei, H., Shen, J., Schoepfer, S.D., Krystyn, L., Richoz, S., Algeo, T.J., 2015. Environmental controls on marine ecosystem recovery following mass extinctions, with an example from the early Triassic. Earth-Science Reviews 149, 108–135. https://doi.org/10.1016/j.earscirev.2014.10.007.
Widmann, P., Bucher, H., Leu, M., Vennemann, T., Bagherpour, B., Schneebeli-Hermann, E., Goudemand, N., Schaltegger, U., 2020. Dynamics of the largest carbon isotope excursion during the early Triassic biotic recovery. Front Earth Sc-Switz 196. https://doi.org/10.3389/feart.2020.00196.
Winchester, J.A., Floyd, P.A., 1977. Geochemical discrimination of different magma series and their differentiation products using immobile elements. Chem. Geol. 20, 325–343. https://doi.org/10.1016/0009-2541(77)90057-2.
Yager, J.A., West, A.J., Thibodeau, A.M., Corsetti, F.A., Rigo, M., Berelson, W.M., Bottjer, D.J., Greene, S.E., Ibarra, Y., Jadoul, F., Ritterbush, K.A., Rollins, N., Rosas, S., Di Stefano, P., Sulca, D., Todaro, S., Wynn, P., Zimmermann, L., Bergquist, B.A., 2021. Mercury contents and isotope ratios from diverse depositional environments across the Triassic-Jurassic Boundary: Towards a more robust mercury proxy for large igneous province magmatism. Earth-Science Reviews 223, 103775. https://doi.org/10.1016/j.earscirev.2021.103775.
Yin, R., Feng, X., Li, X., Yu, B., Du, B., 2014. Trends and advances in mercury stable isotopes as a geochemical tracer. Trends in Environmental Analytical Chemistry 2, 1–10. https://doi.org/10.1016/j.teac.2014.03.001.
Yin, R., Feng, X., Hurley, J.P., Krabbenhoft, D.P., Lepak, R.F., Hu, R., Zhang, Q., Li, Z., Bi, X., 2016. Mercury Isotopes as Proxies to Identify sources and Environmental Impacts of Mercury in Sphalerites. Sci. Rep. 6, 18686. https://doi.org/10.1038/srep18686.
Yin, R., Chen, D., Pan, X., Deng, C., Chen, L., Song, X., Yu, S., Zhu, C., Wei, X., Xu, Y., Feng, X., Blum, J.D., Lehmann, B., 2022. Mantle Hg isotopic heterogeneity and evidence of oceanic Hg recycling into the mantle. Nat. Commun. 13, 948. https://doi.org/10.1038/s41467-022-28577-1.
Zambardi, T., Sonke, J.E., Toutain, J.P., Sortino, F., Shinohara, H., 2009. Mercury emissions and stable isotopic compositions at Vulcano Island (Italy). Earth Planet. Sci. Lett. 277, 236–243. https://doi.org/10.1016/j.epsl.2008.10.023.
Zhang, H., Zhang, F., Chen, J.B., Erwin, D.H., Syverson, D.D., Ni, P., Rampino, M., Chi, Z., Cai, Y.F., Xiang, L., Li, W.Q., Liu, S.A., Wang, R.C., Wang, X.D., Feng, Z., Li, H.M., Zhang, T., Cai, H.M., Zheng, W., Cui, Y., Zhu, X.K., Hou, Z.Q., Wu, F.Y., Xu, Y.G., Planavsky, N., Shen, S.Z., 2021. Felsic volcanism as a factor driving the end-Permian mass extinction. Sci. Adv. 7, eabh1390. https://doi.org/10.1126/sciadv.abh1390.
Zhang, L., Orchard, M.J., Brayard, A., Algeo, T.J., Zhao, L., Chen, Z.-Q., Lyu, Z., 2019. The Smithian/Spathian boundary (late early Triassic): a review of ammonoid, conodont, and carbon-isotopic criteria. Earth Sci 195, 7–36. https://doi.org/10.1016/j.earscirev.2019.02.014.
Zhao, Z., Li, S., Wang, G., Gao, J., Yang, T., Li, Y., He, Z., 2021. Provenance of the Permian–Triassic boundary volcanic ash beds in South China. Geol. J. 56, 2816–2828. https://doi.org/10.1002/gj.4072.
Zi, J.-W., Cawood, P.A., Fan, W.-M., Tohver, E., Wang, Y.-J., McCuaig, T.C., Peng, T.-P., 2013. Late Permian-Triassic magmatic evolution in the Jinshajiang orogenic belt, SW China and implications for orogenic processes following closure of the Paleo-Tethys. Am. J. Sci. 313, 81–112. https://doi.org/10.2475/02.2013.02.